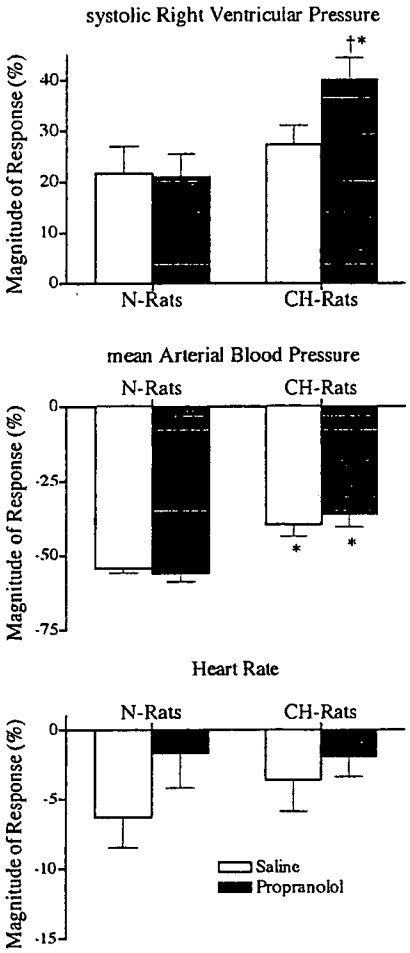

Fig. 6. Hemodynamic responses (% change) of N-rats (n = 5) and CH-rats (n = 5) to acute hypoxia (8% O_2 for 4 min) before and after intravenous administration of propranolol (2 mg/kg). *Significant difference in the magnitude of response between N-rats and CH-rats ($P < 0.05$). †Significant response to propranolol ($P < 0.01$).

underlying mechanisms governing the pathogenesis of PAH remain to be fully elucidated. Specifically, anatomic and structural changes within the pulmonary vascular bed during chronic hypoxia remain unclear.

On the basis of the early work of Reid and colleagues (8, 11, 12, 25), it had become accepted that a reduction in the number of perfused vessels within the pulmonary circulation was an important structural pathology that contributed to the sustained increase in vascular resistance during the pathogenesis of PAH. The reduction in perfused vessels was attributed to either the encroachment of smooth muscle into the vessel lumen, thereby occluding blood flow, or by a reduction in the total number of vessels (i.e., pruning).

One limitation of these studies was the inability to clearly identify the region of susceptibility and the degree of pruning or reduced perfusion. Indeed, because of the limited resolution of conventional X-ray systems, the lung had to first be excised for angiography and then pruning was nonquantitatively described from crude angiographs as a decrease in "background haze" or "background filling" (representing small peripheral vessels) (11, 21, 30).

We (32) have previously described the high definition achieved with SR microangiography for visualizing pulmonary microvessels, with an internal diameter >80 μm. In this study, using SR, we were able to confirm that exposure to chronic hypoxia for 4 wk reduced the number of opaque arterioles with internal diameter >80 μm within the pulmonary circulation. Unlike previous studies, this study was also able to identify the region of susceptibility (i.e., third to fourth generation of branching, 100–300 μm) and to quantify the degree of change (e.g., CH-rats had 47% fewer opaque vessels of the third generation than N-rats) within a closed-chest model, i.e., under intact neurohumoral regulation. One significant limitation with SR, however, is that it is not possible to determine whether the reduction in the number of opaque vessels is due to *1*) pruning of vessels, *2*) occlusion of existing vessels (i.e., complete encroachment of smooth muscle within the vessel lumen), or *3*) partial occlusion, reducing the internal diameter below the resolution limit of SR (i.e., 80 μm).

In the latter case, vessels would still be perfused but would not be visualized by SR. Consequently, the change in the number of perfused microvessels could potentially be overestimated, since we were unable to distinguish between completely occluded and partially occluded vessels. Without further improvements in the signal-to-noise ratio of pixel areas containing fifth-generation branches, it is presently not possible to quantify to what extent the microvessels are perfused in the CH-rat model.

The lung is one of the most densely vascularized organs; therefore, it is extremely difficult to accurately quantify the number of vessels within the "whole" lung. Some studies have claimed that casting techniques, which apply a high-perfusion pressure to distend and fill all arteries to the level of the capillaries, provides evidence that chronic hypoxic reduces vessel number, supporting the concept of pruning (11, 30). However, the reduction of the number of vessels filled with medium within a cast may simply be the result of occlusion, rather than the loss of vessels.

In the past 5 yr, the paradigm of vessel pruning during chronic hypoxia has been challenged, with some reports indicating that the pulmonary circulation appears to undergo angiogenesis during chronic hypoxia (13, 14, 16). However, the vascular region of angiogenesis is uncertain but is likely to occur (if at all) within the capillary bed and/or venules (not the arterioles) because these are the regions of angiogenesis within the systemic circulation (6, 28, 29). Unfortunately, visualizing the capillary network of the lung is presently beyond the resolution capabilities of SR with iodinized contrast agents.

Limitations of this study. Our group has previously described the limitations of SR for visualizing pulmonary vessels <80 μm but also reported that, despite this limitation, a majority of vessels that are susceptible to pathological disorders, and that significantly contribute to an increase in vascular resistance, generally have an internal diameter between 50 and <300 μm (11, 32, 37, 40), i.e., resistance vessels that are at least partially muscular (12). However, resistance vessels <70 μm and lacking complete muscular media also constrict in response to hypoxia (10, 27) and therefore are also likely to be susceptible to pathological changes.

When analyzing the vasoconstriction response to acute hypoxia, we could only analyze vessels with an internal caliber >100 μm because vasoconstriction of vessels <100 μm re-

duced their caliber below the resolution capabilities of SR (i.e., <80 μm).

Another significant limitation of this study is the inability of SR to assess the integrity of the pulmonary arterial vascular wall. Numerous studies have reported that pulmonary vascular remodeling and medial thickening during chronic exposure are significant structural pathologies responsible for the increase in vascular resistance (12, 23, 24, 31). Assessment of vascular remodeling often necessitates histochemical analysis. On the other hand, SR is only able to measure the internal diameter of perfused vessels (assuming the vessel contains sufficient contrast medium) and is therefore a simple, albeit useful, method for assessing gross anatomic changes in the pulmonary circulation of the hypertensive lung. Important information concerning vascular wall thickness and medial thickening cannot be assessed with SR.

In this study, we could not view the circulation of the whole lung; rather, we were restricted to a relatively small field of view of 9.5 × 9.5 mm. We therefore make the assumption that the image captured within the 9 × 9 window is representative of the whole lung circulation. However, changes in vascular resistance (during either acute of chronic hypoxia) are the consequence of global pulmonary vasoconstriction and/or remodeling.

HPV in the rat. In this study, we used SR to assess the dynamic changes in vessel caliber during acute hypoxia (i.e., HPV). The results of this study concur with our previous report (32) that showed, in N-rats, that all vessels with a diameter <500 μm, especially between 200 and 300 μm, constricted in response to acute hypoxia (8% O_2). The unique result of this study is that chronic hypoxia did not significantly alter HPV, as assessed by hemodynamic and microangiography analysis.

HPV has been reported to preferentially occur in vessels with an internal diameter of ~150–300 μm in cats and rabbits (17, 34, 35) and rats (32) and up to 600 μm in dogs (1). Chronic hypoxia has been reported to alter acute HPV due to structural changes in the pulmonary vasculature (22). According to the literature, chronic hypoxia can potentially attenuate (9, 15, 38, 41), enhance, or have no effect on the acute HPV (5, 7, 18). Despite decades of research concerning HPV, the exact mechanism(s) that governs acute HPV is yet to be fully elucidated, although various humoral (e.g., nitric oxide) and neural pathways are likely to be involved [see Moudgil et al. (26) for a review]. In this study, we aimed to specifically assess sympathetic modulation of the HPV by SR microangiography. Although sympathetic fibers innervate the pulmonary vasculature, neural control of "tonic" pulmonary vascular tone is less prominent than that of the systemic vasculature. However, modulation of the pulmonary vasculature by the sympathetic nervous system becomes critically important under stressful conditions, such as hypoxia (33, 35).

Hypoxia is a potent activator of pulmonary sympathetic nerve activity. The increase in sympathetic nerve activity has been reported to attenuate the local vasoconstrictor effects of hypoxia via a β-adrenoceptor-mediated vasodilator mechanism, especially when the inspired level of O_2 is ≤8% O_2 (33, 35). For example, Shirai et al. (35) reported that HPV was greater for moderate (10% O_2) than for severe hypoxia (5% O_2), but only if the hypoxia was global (i.e., whole body). If the hypoxic stimulus was restricted to just the lung (i.e., regional hypoxia), the magnitude of vasoconstriction was proportional to the degree of hypoxia (i.e., greatest for 5% O_2). Shirai et al. (35) subsequently demonstrated that the vasoconstrictor response to severe global hypoxia is offset by a sympathetic β-adrenoceptor-mediated vasodilatory mechanism.

In our study, we observed that sympathetic β-adrenoceptor blockade (using propranolol) in N-rats did not modify baseline vascular tone, but it did accentuate HPV of those vessels 200–300 μm in diameter. These results support the concept that modulation of the pulmonary vasculature by the sympathetic nervous system appears to be an important homeostatic response for limiting the magnitude of vasoconstriction under hypoxic conditions.

Interestingly, although β-adrenoceptor blockade accentuated HPV in this study, it did not significantly alter the magnitude of the systolic RVP to acute hypoxia in N-rats. This difference may be attributed to a decrease in cardiac output (not measured in this study), since β-receptor blockade has been reported to significantly reduce cardiac output (4, 20). Alternatively, the magnitude of vasoconstriction may not have been sufficient to elicit a significant change in the systolic RVP response, since *1*) propranolol accentuated the HPV of only the 200- to 300-μm vessels and *2*) the vasoconstriction observed within the 9.5 × 9.5-mm field of view may not be representative of the whole lung (as discussed above).

The mechanism(s) responsible for alterations of the HPV after chronic hypoxia remains poorly understood. In this study, we observed that β-receptor blockade in CH-rats significantly accentuated the HPV, not only in the 200- to 300-μm vessels as observed in N-rats but also in the 100- to 200-μm vessels. Consequently, the systolic RVP response to acute hypoxia was also enhanced by propranolol. These results indicate that sympathetic modulation of the HPV becomes critically enhanced after chronic hypoxia.

Although the mechanisms for these observations need to be further researched, we speculate that the enhanced HPV may be attributable to *1*) the formation of new muscle around nonmuscular or partially muscular vessels (50–150 μm) and *2*) an increase in sympathetic innervation of the pulmonary vasculature. HPV is intrinsic to the lung, and, although modulated by the endothelium, the core mechanism is in the smooth muscle cell (26). Peripheral arterioles undergo medial thickening during chronic hypoxia. Therefore, in this study, it may be possible that the potential of the 100- to 200-μm vessels to constrict was enhanced after chronic hypoxia. However, the difference in the vasoconstrictive response of 100- to 200-μm vessels between N-rats and CH-rats was only apparent after β-receptor blockade. Studies have shown that chronic hypoxia significantly increases β-receptor number within the lung (3, 39), so that modulation of HPV by the sympathetic nervous system is enhanced after chronic hypoxia. These reports are in agreement with the observations of this study.

Future directions. The primary aim of this study was to demonstrate the effectiveness of SR for "visualizing" the pathological changes in pulmonary microcirculation in a closed-chest rat model after the development of pulmonary hypertension. As a result, this study has provided a foundation with which future investigative studies can build to further elucidate the adverse changes in the pulmonary circulation during hypertension. Specifically, we used only one stimulant (acute hypoxia) to test the reactivity of the pulmonary circulation. However, the question still remains as to whether

reactivity to other specific vasoactive agents is altered in hypertension (e.g., reactive oxygen species, nitric oxide, endothelin-1, etc.) and what region of the microcirculation is most susceptible to pathological changes (i.e., vessel branching generation and vessel size). Ultimately, it is anticipated that SR will provide an effective means of assessing potential therapeutic or prophylactic treatments for PAH.

In summary, we have demonstrated the effectiveness of SR for assessing changes in pulmonary blood flow distribution and functional changes (i.e., HPV) associated with the pathogenesis of PAH. Despite some limitations, the observations from this study can provide future direction for investigating the potential mechanisms responsible for these pathological changes. Of particular importance, future use of SR will provide an effective method for assessing the potential treatments for PAH.

ACKNOWLEDGMENTS

The SR experiments were performed at the BL28B2 in the SPring-8 with the approval of the Japan Synchrotron Radiation Research Institute (Proposal 2006BO464-NL2-NP).

GRANTS

This study was supported in part by the "Program for Promotion of Fundamental Studies in Health Sciences of the National Institute of Biomedical Innovation (NIBIO)" and also in part by a Grant-in-Aid for Scientific Research (16659210) and a Monash Synchrotron Fellowship (J. T. Pearson). We also acknowledge financial support from the access to Major Research Facilities Programme, which is a component of the International Science Linkages Programme (Australian Government).

REFERENCES

1. **Al-Tinawi A, Krenz GS, Rickaby DA, Linehan JH, Dawson CA.** Influence of hypoxia and serotonin on small pulmonary vessels. *J Appl Physiol* 76: 56–64, 1994.
2. **Archer S, Rich S.** Primary pulmonary hypertension: a vascular biology and translational research "Work in progress." *Circulation* 102: 2781–2791, 2000.
3. **Birnkrant DJ, Davis PB, Ernsberger P.** Visualization of high- and low-affinity β-adrenergic receptors in rat lung: upregulation by chronic hypoxia. *Am J Physiol Lung Cell Mol Physiol* 265: L389–L394, 1993.
4. **Chiong MA, Hatcher JD.** The sympathoadrenergic system in the cardiovascular responses to hypoxia in the dog. *Can J Physiol Pharmacol* 50: 674–683, 1972.
5. **Clini E, Cremona G, Campana M, Scotti C, Pagani M, Bianchi L, Giordano A, Ambrosino N.** Production of endogenous nitric oxide in chronic obstructive pulmonary disease and patients with cor pulmonale. Correlates with echo-Doppler assessment. *Am J Respir Crit Care Med* 162: 446–450, 2000.
6. **Diaz-Flores L, Gutierrez R, Varela H.** Angiogenesis: an update. *Histol Histopathol* 9: 807–843, 1994.
7. **Emery CJ, Bee D, Barer GR.** Mechanical properties and reactivity of vessels in isolated perfused lungs of chronically hypoxic rats. *Clin Sci (Lond)* 61: 569–580, 1981.
8. **Fried R, Reid LM.** Early recovery from hypoxic pulmonary hypertension: a structural and functional study. *J Appl Physiol* 57: 1247–1253, 1984.
9. **Hampl V, Archer SL, Nelson DP, Weir EK.** Chronic EDRF inhibition and hypoxia: effects on pulmonary circulation and systemic blood pressure. *J Appl Physiol* 75: 1748–1757, 1993.
10. **Hillier SC, Graham JA, Hanger CC, Godbey PS, Glenny RW, Wagner WWJ.** Hypoxic vasoconstriction in pulmonary arterioles and venules. *J Appl Physiol* 82: 1084–1090, 1997.
11. **Hislop A, Reid L.** New findings in pulmonary arteries of rats with hypoxia-induced pulmonary hypertension. *Br J Exp Pathol* 57: 542–554, 1976.
12. **Hislop A, Reid L.** Normal structure and dimensions of the pulmonary arteries in the rat. *J Anat* 125: 71–83, 1978.
13. **Hopkins N, McLoughlin P.** The structural basis of pulmonary hypertension in chronic lung disease: remodelling, rarefaction or angiogenesis? *J Anat* 201: 335–348, 2002.
14. **Howell K, Preston RJ, McLoughlin P.** Chronic hypoxia causes angiogenesis in addition to remodelling in the adult rat pulmonary circulation. *J Physiol* 547: 133–145, 2003.
15. **Huang KL, Wu CP, Kang BH, Lin YC.** Chronic hypoxia attenuates nitric oxide-dependent hemodynamic responses to acute hypoxia. *J Biomed Sci* 9: 206–212, 2002.
16. **Hyvelin J, Howell K, Nichol A, Costello CM, Preston RJ, McLoughlin P.** Inhibition of Rho-kinase attenuates hypoxia-induced angiogenesis in the pulmonary circulation. *Circ Res* 97: 185–191, 2005.
17. **Ikai A, Shirai M, Nishimura K, Ikeda T, Kameyama T, Ueyama K, Komeda M.** Maintenance of pulmonary vasculature tone by blood derived from the inferior vena cava in a rabbit model of cavopulmonary shunt. *J Thorac Cardiovasc Surg* 129: 199–206, 2005.
18. **Karamsetty VS, MacLean MR, McCulloch KM, Kane KA, Wadsworth RM.** Hypoxic constrictor response in the isolated pulmonary artery from chronically hypoxic rats. *Respir Physiol* 105: 85–93, 1996.
19. **Kelly DA, Hislop AA, Hall SM, Haworth SG.** Relationship between structural remodeling and reactivity in pulmonary resistance arteries from hypertensive piglets. *Pediatr Res* 58: 525–530, 2005.
20. **Kontos HA, Lower RR.** Role of β-adrenergic receptors in the circulatory response to hypoxia. *Am J Physiol* 217: 756–763, 1969.
21. **Le Cras TD, Markham NE, Tuder RM, Voelkel NF, Abman SH.** Treatment of newborn rats with a VEGF receptor inhibitor causes pulmonary hypertension and abnormal lung structure. *Am J Physiol Lung Cell Mol Physiol* 283: L555–L562, 2002.
22. **McMurtry IF, Petrun MD, Reeves JT.** Lungs from chronically hypoxic rats have decreased pressor response to acute hypoxia. *Am J Physiol Heart Circ Physiol* 235: H104–H109, 1978.
23. **Meyrick B, Fujiwara K, Reid L.** Smooth muscle myosin in precursor and mature smooth muscle cells in normal pulmonary arteries and the effect of hypoxia. *Exp Lung Res* 2: 303–313, 1981.
24. **Meyrick B, Hislop A, Reid L.** Pulmonary arteries of the normal rat: the thick walled oblique muscle segment. *J Anat* 125: 209–221, 1978.
25. **Meyrick B, Reid L.** The effect of continued hypoxia on rat pulmonary arterial circulation. An ultrastructural study. *Lab Invest* 38: 188–200, 1978.
26. **Moudgil R, Michelakis ED, Archer SL.** Hypoxic pulmonary vasoconstriction. *J Appl Physiol* 98: 390–403, 2005.
27. **Nagasaka Y, Bhattacharya J, Nanjo S, Gropper MA, Staub NC.** Micropuncture measurement of lung microvascular pressure profile during hypoxia in cats. *Circ Res* 54: 90–95, 1984.
28. **Patan S.** Vasculogenesis and angiogenesis. *Cancer Treat Res* 117: 3–32, 2004.
29. **Patan S, Munn LL, Tanda S, Roberge S, Jain RK, Jones RC.** Vascular morphogenesis and remodeling in a model of tissue repair: blood vessel formation and growth in the ovarian pedicle after ovariectomy. *Circ Res* 89: 723–731, 2001.
30. **Rabinovitch M, Gamble W, Nadas AS, Miettinen OS, Reid L.** Rat pulmonary circulation after chronic hypoxia: hemodynamic and structural features. *Am J Physiol Heart Circ Physiol* 236: H818–H827, 1979.
31. **Sasaki S, Kobayashi N, Dambara T, Kira S, Sakai T.** Structural organization of pulmonary arteries in the rat lung. *Anat Embryol (Berl)* 191: 477–489, 1995.
32. **Schwenke DO, Pearson JT, Kangawa K, Umetani K, Shirai M.** Imaging of the pulmonary circulation in the closed-chest rat using synchrotron radiation microangiography. *J Appl Physiol* 102: 787–793, 2007.
33. **Shirai M, Matsukawa K, Nishiura N, Kawaguchi AT, Ninomiya I.** Changes in efferent pulmonary sympathetic nerve activity during systemic hypoxia in anesthetized cats. *Am J Physiol Regul Integr Comp Physiol* 269: R1404–R1409, 1995.
34. **Shirai M, Shimouchi A, Kawaguchi AT, Sunagawa K, Ninomiya I.** Inhaled nitric oxide: diameter response patterns in feline small pulmonary arteries and veins. *Am J Physiol Heart Circ Physiol* 270: H974–H980, 1996.
35. **Shirai M, Shindo T, Ninomiya I.** β-Adrenergic mechanisms attenuated hypoxic pulmonary vasoconstriction during systemic hypoxia in cats. *Am J Physiol Heart Circ Physiol* 266: H1777–H1785, 1994.
36. **Tanaka A, Mori H, Tanaka E, Mohammed MU, Tanaka Y, Sekka T, Ito K, Shinozaki Y, Hyodo K, Ando M, Umetani K, Tanioka K, Kubota M, Abe S, Handa S, Nakazawa H.** Branching patterns of intramural coronary vessels determined by microangiography using synchrotron radiation. *Am J Physiol Heart Circ Physiol* 276: H2262–H2267, 1999.
37. **Tokiya R, Umetani K, Imai S, Yamashita T, Hiratsuka J, Imajo Y.** Observation of microvasculatures in athymic nude rat transplanted tumor

using synchrotron radiation microangiography system. *Acad Radiol* 11: 1039–1046, 2004.

38. **Weissmann N, Nollen M, Gerigk B, Ardeschir Ghofrani H, Schermuly RT, Gunther A, Quanz K, Fink L, Hanze J, Rose F, Seeger W, Grimminger F.** Downregulation of hypoxic vasoconstriction by chronic hypoxia in rabbits: effects of nitric oxide. *Am J Physiol Heart Circ Physiol* 284: H931–H938, 2003.
39. **Winter RJ, Dickinson KE, Rudd RM, Sever PS.** Tissue specific modulation of β-adrenoceptor number in rats with chronic hypoxia with an attenuated response to down-regulation by salbutamol. *Clin Sci (Lond)* 70: 159–165, 1986.
40. **Yamashita T, Kawashima S, Ozaki M, Namiki M, Shinohara M, Inoue N, Hirata K, Umetani K, Yokoyama M.** In vivo angiographic detection of vascular lesions in apolipoprotein E-knockout mice using a synchrotron radiation microangiography system. *Circ J* 66: 1057–1059, 2002.
41. **Zhao L, Crawley DE, Hughes JM, Evans TW, Winter RJ.** Endothelium-derived relaxing factor activity in rat lung during hypoxic pulmonary vascular remodeling. *J Appl Physiol* 74: 1061–1065, 1993.

Synchrotron Radiation Coronary Microangiography for Morphometric and Physiological Evaluation of Myocardial Neovascularization Induced by Endothelial Progenitor Cell Transplantation

Hiroto Iwasaki, Kazuhito Fukushima, Atsuhiko Kawamoto, Keiji Umetani, Akira Oyamada, Saeko Hayashi, Tomoyuki Matsumoto, Masakazu Ishikawa, Toshihiko Shibata, Hiromi Nishimura, Hidekazu Hirai, Yutaka Mifune, Miki Horii, Kazuro Sugimura, Shigefumi Suehiro, Takayuki Asahara

Background—Therapeutic effect of stem cell transplantation (SCTx) for myocardial neovascularization has been evaluated by histological capillary density in small animals. However, it has been technically difficult to obtain imaging evidence of collateral formation by conventional angiography.

Methods and Results—Peripheral blood CD34+ and CD34− cells were isolated from patients with critical limb ischemia. PBS, CD34− cells, or CD34+ cells were intramyocardially transplanted after ligating LAD of nude rats. Coronary angiography of ex vivo beating hearts 5 and 28 days after the treatment was performed using the third generation synchrotron radiation microangiography (SRM), which has potential to visualize vessels as small as 20 μm in diameter. The SRM was performed pre and post sodium nitroprusside (SNP) to examine vascular physiology at each time point. Diameter of most collateral vessels was 20 to 120 μm, apparently invisible size in conventional angiography. Rentrop scores at day 28 pre and post SNP were significantly greater in CD34+ cell group than other groups ($P<0.01$). To quantify the extent of collateral formation, angiographic microvessel density (AMVD) in the occluded LAD area was analyzed. AMVD on day 28 post SNP, not pre SNP, was significantly augmented in CD34+ cell group than other groups ($P<0.05$). AMVD post SNP closely correlated with histological capillary density ($R=0.82$, $P<0.0001$).

Conclusions—The SRM, capable of visualizing microvessels, may be useful for morphometric and physiological evaluation of coronary collateral formation by SCTx. The novel imaging system may be an essential tool in future preclinical/translational research of stem cell biology. (***Arterioscler Thromb Vasc Biol.* 2007;27:1326-1333.**)

Key Words: synchrotron radiation microangiography ■ image ■ CD34+ cells ■ neovascularization ■ myocardial infarction

Stem/progenitor cell transplantation (SCTx) investigated since the early 1990s is a novel approach for vascular regeneration therapy in ischemic diseases.[1–3] One of the examples of the SCTx is transplantation of adult peripheral blood CD34+ cells that are endothelial progenitor cell (EPC)-enriched population. Transplantation of CD34+ cells prevents left ventricular (LV) dilatation and wall thinning, inhibits myocardial fibrosis and apoptosis, and preserves LV function through augmentation of myocardial neovascularization and blood flow.[4–9] Evidence of increased vascularity by therapeutic neovascularization such as CD34+ cell transplantation has been obtained by histological assessment of capillary density and physiological evaluation of tissue perfusion has been by microsphere methods in small sized animals (mice and rats) with acute MI.[10] However, the histological examination has limitation for precise assessment of vascular physiology in response to environmental stress. Though microsphere assessment was performed to evaluate physiological blood flow, it was pointed out to lack significant reproducibility in small animal models. Several research groups have utilized other approaches such as corrosion casts[11,12] and angiography[13,14] to visualize collateral vessels.

Original received November 29, 2006; final version accepted February 12, 2007.

From Stem Cell Translational Research (H.I., A.K., A.O., S.H., T.M., M.I., H.N., Y.M., M.H., T.A.), Kobe Institute of Biomedical Research and Innovation/RIKEN Center for Developmental Biology; the Department of Cardiovascular Surgery (H.I., T.S., H.H., S.S.), Osaka City University Graduate School of Medicine; the Department of Image-based Medicine (K.F.), Kobe Institute of Biomedical Research and Innovation; the Department of Radiology (K.F., K.S.), Kobe University Graduate School of Medicine; the Research & Utilization Division (K.U.), Japan Synchrotron Radiation Research Institute, SPring-8, Sayo; and the Department of Regenerative Medicine Science (T.A.), Tokai University School of Medicine, Isehara, Japan.

H.I. and K.F. contributed equally to this work.

Correspondence to Takayuki Asahara, MD, Stem Cell Translational Research, Kobe Institute of Biomedical Research and Innovation/RIKEN Center for Developmental Biology, 2-2 Minatojima-Minamimachi, Chuo-ku, Kobe 650-0047, Japan. E-mail asa777@aol.com

Arterioscler Thromb Vasc Biol. **is available at http://www.atvbaha.org** **DOI: 10.1161/ATVBAHA.106.137141**

Corrosion casts allow the visualization of small arteries less than 100 μm in diameter,[11] although it is impossible to examine in live animals or ex vivo beating hearts, and the complete distension of the vessels depends on several factors such as elastic properties of the vessel wall, viscosity of the infused material, and pressure of infusion. Conventional angiography, which has been widely performed in clinical practice, can be also undergone in live animals repeatedly. However, previous reports indicated that conventional angiography systems, which could not visualize arteries less than 200 μm in diameter,[15,16] have insufficient resolution to visualize full extent of collateral formation. The resolutional limitation may lead to underestimation of angiogenic potential of the SCTx, because improvement of collateral-dependent flow typically results from the proliferation of vessels less than 180 μm in diameter.[17–19] The indispensable angiographic assessment in small animals has never been established.

Synchrotron radiation (SR) has been investigated as a novel approach for animal studies because intravenous coronary angiography, a relatively less invasive technique compared with selective coronary angiography, was begun at the end of 1970's. Research groups have improved imaging systems in SR facilities for future clinical application.[20] Aside from the intravenous coronary angiography, Mori et al[15,16] recently developed a new angiography system called SR microangiography (SRM), which was an intraarterial microangiography system. In this system, monochromatic SR is used as an x-ray source, which energy was adjusted to 33.2 keV just above the iodine K-edge energy to produce the highest contrast image of the iodine contrast material, and a high-fidelity video system is also used as a detector, which has the potential to visualize small vessels (diameter <50 to 100 μm). Thereafter, many researchers have used the SRM to visualize penetrating transmural coronary arteries in the canine hearts,[21] collateral microvessels following therapeutic angiogenesis in rat model of hind limb ischemia,[22] vasodilatation of arterial circle of cerebrum and its branches of the dogs,[23] and tumor-derived angiogenic vessels of the rabbits[24] at the Photon Factory in Tsukuba, Japan. However, the previous SRM system was unable to visualize coronary arteries, their branches, and collateral vessels in beating hearts of small animals because of the still inappropriate image quality. Currently, new SRM system with spatial resolution in the μm range has been developed in the SPring-8 (Japan Synchrotron Radiation Research Institute) in Sayo, Japan. Recently, Kidoguchi et al[25] have applied the new SRM system to visualize branches of rat middle cerebral arteries and successfully depict the vessels as small as 30 μm in diameter at 9.5 μm of detector pixel size. In this study, we used the new generation SRM to visualize rat coronary vessels as small as 20 μm in diameter at 4.5 μm of pixel size and evaluated coronary vascular function in response to vasodilator under fast beating condition. Here, we report usefulness of the third generation SRM to visualize collateral vessels and quantify the effect of therapeutic neovascularization by bone marrow (BM)-derived CD34+ cell transplantation in rats with MI.

Methods

Isolation of CD34+ Cells From Patients With Critical Limb Ischemia

Peripheral blood total mononuclear cells (tMNCs) were obtained from 3 male patients 71, 63, and 60 years of age with atherosclerotic peripheral artery disease by apheresis after 5-day subcutaneous administration of G-colony stimulating factor (CSF) (10 μg/kg/d). CD34+ cells or CD34− cells were isolated from the tMNCs by a magnetic cell sorting system, CliniMACS (Miltenyi Biotec).[26] The CD34+ cell fraction had a purity of >99%, as determined by fluorescence-activated cell sorting (FACS) analysis using a monoclonal antibody specific for human CD34 (Becton Dickinson). CD34+ cells in this study were $CD31^{bright}$, $AC133^{bright}$, and $CD45^{dim}$ but negative for KDR and VE-cadherin. In contrast, CD34− cells were positive for CD45 and CD31, but negative for AC133, KDR, and VE-cadherin. The FACS results suggest that freshly-isolated CD34+ cells are immature population responsible for hematopoietic stem cells, endothelial progenitor cells, and hemangioblasts, whereas the CD34− cells are not considered to be either immature or mature endothelial lineage cells (supplemental Figure I, available online at http://atvb.ahajournals.org).

These patients received intramuscular transplantation of 10^5 CD34+ cells/kg according to the protocol of a phase I/II dose-escalation clinical trial. Remaining CD34+ or CD34− cells were used for following experiments. Informed consent regarding the cell therapy and experimental use of the remaining cells was obtained from each patient before the case registration. The clinical study protocol was approved by the Institutional Ethics Committees of Kobe Institute of Biomedical Research and Innovation and Kobe City General Hospital.

Animals

Female athymic nude rats (F344/N Jcl rnu/rnu; CLEA Japan, Tokyo, Japan) aged 7 to 8 weeks and weighing 145–160 g were used in this study. The Institutional Animal Care and Use Committees of RIKEN Center for Developmental Biology approved all animal procedures including human cell transplantation. All of our experiments on imaging of the rat hearts with MI also conformed to the SPring-8 Guide for Care and Use of Laboratory Animals in SRM examination.

Induction of Myocardial Infarction and Cell Transplantation

Rats were anesthetized with ketamine and xylazine (60 mg/kg and 10 mg/kg, respectively, IP). MI was induced by ligating left anterior descending coronary artery (LAD) as described previously.[7–9] Twenty minutes after MI, rats received intramyocardial transplantation of 1×10^5 CD34− cells or 1×10^5 CD34+ cells resuspended with 100 μL of PBS or the same volume of PBS without cells (n=9 in each group). To evaluate incorporation and development of the transplanted cells in MI tissue, CD34+ cells or CD34− cells labeled with fluorescent carbocyamine 1, 1′-dioctadecyl1–1 to 3,3,3,3′-tetramethylindocarbocyanine perchlorate (DiI) dye (Molecular Probes, Carlsbad, CA) were intramyocardially transferred into athmic nude rats (n=3) after MI.[9]

Imaging System

SRM experiments were performed at the 2nd optical hatch of the BL28B2 beamline in the SPring-8. Monochromatic synchrotron radiation with an energy level of 33.2 keV was obtained from the beamline. An X-ray imaging system needs to have high shutter speed to make sharp and blur-free images of fast-moving hearts, and for this purpose we developed a shutter system using a rotating disk with radial slots rotating around an axis parallel to the X-ray beam. The shortest shutter open time was 0.1 ms. X-rays transmitted through the object are detected by the X-ray direct-conversion type detector incorporating the X-ray SATICON pick-up tube. For high-resolution, real-time imaging (7.0 μm or 4.5 μm pixel size, 30 frames/second), the monochromatized x-ray obtained from the third generation SR source and the new rotating disk shatter were used.

Differences in Characteristics of Synchrotron Radiation System Between the Photon Factory and the SPring-8

	Photon Factory	SPring-8
Input field of view, mm	50×50 or 20×20	7.0×7.0 or 4.5×4.5
Pixel size, μm	48×48 or 19×19	7.×7.0 or 4.5×4.5
Spatial resolution, μm	30	6
Minimum detectable vessel diameter, μm	50–100	20
Shortest shutter open time, msec	17	2

Sequential images were obtained with an input field of view of 7.0 mm × 7.0 mm or 4.5 mm × 4.5 mm. Image signals were converted into digital format and stored in a frame memory with a 1024×1024 pixels format and 10-bit resolution. Improved points in the new generation SR imaging system in the Spring-8 compared with the previous version in the Photon Factory in Tsukuba, Japan is shown in the Table.

Coronary Microangiography

Transplanted immunodeficient rats were anesthetized with pentobarbital and anticoagulant heparin intraperitoneally. After thoracotomy, the heart and aortic arch were rapidly excised and immersed in perfusion solution. The pericardium was quickly removed under immersion and aorta was prepared for cannulation. The heart was mounted on an aortic cannula, and then pulmonary artery was cut near its origin. Throughout the experiment, aortic retrograde perfusion at a constant flow rate (4.0 mL/min) with oxygenated perfusion solution drawn from a temperature-regulated reservoir (37°C) was started according to the Langendorf technique, as described in detail previously.[27] The perfusion solution was of the following composition (in mmol/L): NaCl, 118.5; $NaHCO_3$, 25.0; KCl, 3.2; $MgSO_4$, 1.2; KH_2PO_4, 1.2; $CaCl_2$, 1.4; glucose, 11.0. The solution was filtered before use and gassed continuously with 90% O_2/10% CO_2 (pH 7.4 at 37°C). Perfusion fluid was directed into coronary arteries to perfuse the entire ventricular mass of the heart. Contractile function and regular heart rhythm returned within a few seconds, and maximum function was established in several minutes. After stabilization of heart rate and perfusion pressure in the ex vivo beating hearts under the Langendorf perfusion, SRM at baseline was performed in each animal. The microangiographic images were taken at base, mitral papillary muscle, and apical levels. Microangiography was performed with an automated injector (Nemoto Kyorindo) which was programmed to reproducibly deliver 0.4 mL/sec of nonionic contrast media containing 37% iodine (Iopamiron 370; Nihon Schering) for 4 sec. After the baseline angiography were taken, sodium nitroprusside (SNP) (Roche), an endothelium-nondependent vasodilator, was added to oxigenized Krebs-Henseleit solution while keeping the perfusate concentrations and the flow rate. The concentration of SNP used in this study was 1×10^{-6} mol/L, which corresponds to values validated as the most suitable concentration of SNP to assess the vasodilating effect in a previous study.[28] Microangiography was similarly performed to visualize dilated coronary vessels. Each imaging started 1 to 2 seconds before contrast media infusion, so that background pictures without contrast media could be taken for later computed analysis.

Tissue Harvest

After SRM, hearts were sliced in a broad-leaf fashion into 4 transverse sections from apex to base, embedded in OCT compound, snap frozen in liquid nitrogen (LN_2), and stored at −80°C for immunohistochemistry. Rat hearts in OCT blocks were sectioned, and 5-μm serial sections were collected on slides followed by fixation with 4.0% paraformaldehyde at 4°C for 5 minutes and stained immediately. Total RNA was isolated by selective dissection of peri-infarct area in LV myocardium for reverse transcriptase-polymerase chain reaction (RT-PCR).

Angiographic Assessment of Collateral Vessel Formation

Collateral flow filling to the LAD territory pre and post SNP was graded angiographically in a blinded manner by use of the Rentrop scoring system.[7] To quantify development of collateral vessels, angiographic microvessel density (AMVD) in the occluded LAD area both pre and post SNP was measured by following computed analysis. Hearts were divided into 4 parts from ligation point to apex, then we measured vessel densities in each part. Region of interest was determined in LAD perfusing area but without visible major branches of the LAD. The images immediate before (background) and during contrast media infusion were captured by an image scanner. After the image capture, vessel density in each part was obtained by subtracting the background density from the angiographic density processed with the NIH image program (v. 1.62) as described previously.[29] Average value of the vessel densities in 4 portions was calculated as the AMVD for each imaging procedure. The ratio of AMVD post SNP to pre SNP (AMVD ratio) was also calculated. These data analyses were performed by 2 blinded observers.

Morphometric Evaluation of Capillary Density

Histochemical staining with isolectin B4 (Vector Laboratories) was performed, and capillaries were recognized as tubular structures positive for isolectin B4. Histological capillary density was evaluated by morphometric examination of 5 randomly selected fields of tissue sections recovered from segments of LV myocardium subserved by the occluded LAD.[7–9] All morphometric studies were performed by 2 examiners who were blinded to treatment.

Statistical Analysis

The results were statistically analyzed with the use of a software package (Statview 5.0, Abacus Concepts Inc). All values were expressed as mean±SE. Paired t tests were performed for comparison of data between day 5 and day 28, and between pre and post SNP infusion. The comparisons among 3 groups were made with 1-way ANOVAs. Post hoc analysis was performed by Fisher protected least significant difference test. Correlation between histological and microangiographic vessel densities was analyzed by linear regression test. Differences of $P<0.05$ were considered statistically significant.

Results

Rentrop Score Pre and Post SNP Infusion

SRM was performed to evaluate collateral vessel development by elucidating Rentrop score, a semiquantitative grading of collateral flow filling into the occluded coronary artery,[10] 5 and 28 days after cell transplantation. SRM on day 5 demonstrated that the LAD was totally occluded at the ligation point and collateral flow filling into the distal LAD was not well visualized in all groups (Figure 1a). Angiographic Rentrop score at day 5 was not significantly different in each group (Figure 1c). In contrast, SRM on day 28 revealed better visualization of collateral vessels into the distal LAD area in CD34+ cell group compared with both CD34− cell and PBS groups. Collateral vessels were generated from left circumflex artery or proximal site of LAD. Diameter of the collateral vessels was generally 20 to 120 μm, which is apparently invisible size in conventional angiography (Figure 2a). Rentrop score at day 28 was significantly greater in CD34+ cell group than either CD34− cell or PBS group (CD34+, 1.6±0.2; CD34−, 0.6±0.2; PBS, 0.4±0.2, $P<0.01$ for CD34+ versus CD34− and PBS) (Figure 2c).

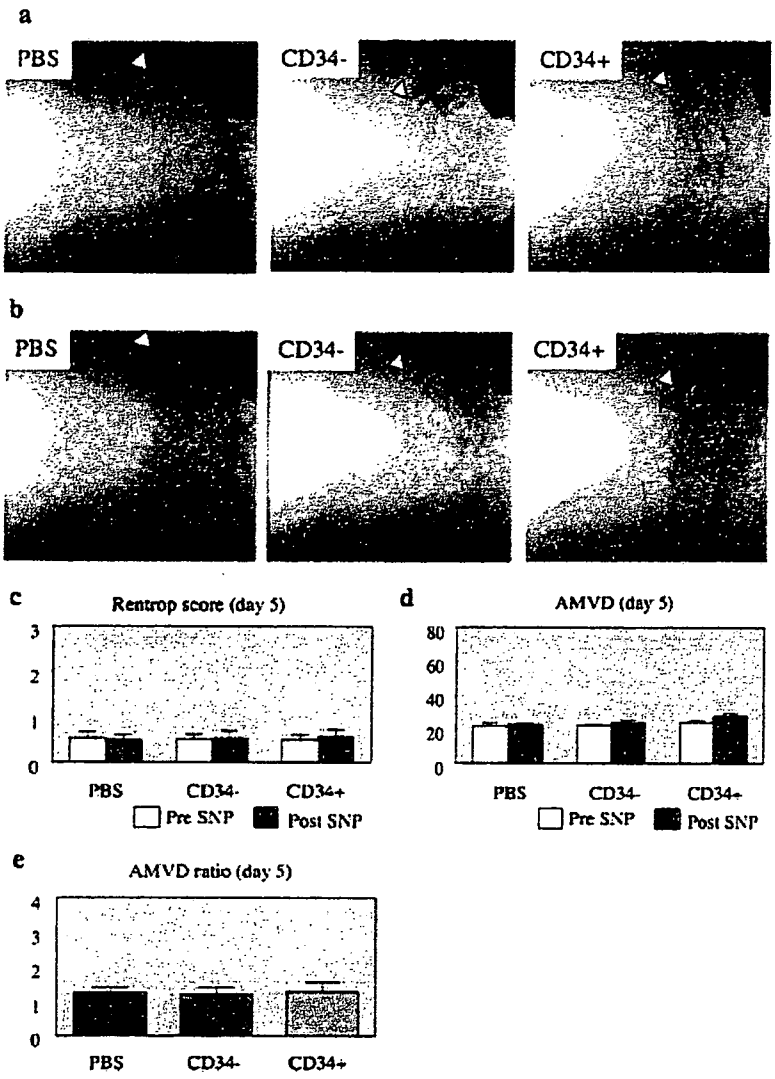

Figure 1. a, Representative images of synchrotron radiation microangiography (SRM) 5 days after PBS, CD34−, or CD34+ cell transplantation (pre sodium nitroprusside [SNP]; 7.0×7.0 mm). Collateral vessels were poorly visualized in all groups. Arrowhead shows ligation point (scale bar; 100 μm). b, Representative SRM images post SNP at day 5 (7.0×7.0 mm). Collateral vessels were poorly visualized in all groups (scale bar; 100 μm). c, Rentrop score of collateral development pre and post SNP in each group at day 5. d, Angiographic microvessel density (AMVD) pre and post SNP in each group at day 5. e, Ratio of AMVD post SNP to pre SNP (AMVD ratio) in each group at day 5.

SRM post SNP was similarly performed to evaluate the augmentation of new microvasculature 5 and 28 days after transplantation. SRM on day 5 revealed slightly better visualization of the new microvasculature post SNP compared with pre SNP in each group (Figure 1b). However, Rentrop score post SNP at day 5 was not significantly different in each group (Figure 1c). SRM on day 28 in CD34+ cell group, not in CD34− and PBS groups, revealed that new microvasculature in the occluded LAD area was better visualized post SNP than pre SNP (Figure 2a and 2b). Rentrop score at day 28 in CD34+ cell group was significantly greater post SNP than pre SNP (CD34+ post SNP, 1.8±0.1; CD34+ pre SNP, 1.6±0.2, $P<0.05$). However, in PBS or CD34− cell group, Rentrop score at day 28 post SNP was not significantly different from that pre SNP (Figure 2c).

SRM post SNP at day 28 revealed better visualization of collateral vessels into the distal LAD area in CD34+ cell group compared with both CD34− cell and PBS groups (Figure 2b). Rentrop score post SNP at day 28 was significantly greater in CD34+ cell group than either CD34− cell or PBS group (CD34+, 1.8±0.1; CD34−, 0.7±0.2; PBS, 0.5±0.2, $P<0.01$ for CD34+ versus CD34− and PBS) (Figure 2c).

Thus, the new generation SRM system enabled visualization and evaluation of new microvasculature created by CD34+ cell transplantation in the fast beating rat hearts. These results suggest that CD34+ cell transplantation may enhance collateral blood flow in the ischemic myocardium and may also improve collateral vascular function in response to SNP infusion.

Angiographic Microvessel Density (AMVD) in SRM

To quantify the activity of collateral vascular formation in the occluded LAD area, we measured the AMVD in SRM by computed analysis. AMVD pre and post SNP on day 5 was not significantly different in CD34+ cell group from that in other groups (Figure 1d). The ratio of AMVD post SNP to pre SNP (AMVD ratio) on day 5 was similar in all groups (Figure 1e).

AMVD pre SNP on day 28 was not significantly different in CD34+ cell group from that in other groups (CD34+, 27.3±3.2; CD34−, 23.2±0.8, PBS, 21.6±2.7). However, in CD34+ cell group, not in other groups, AMVD on day 28 was significantly greater post SNP than

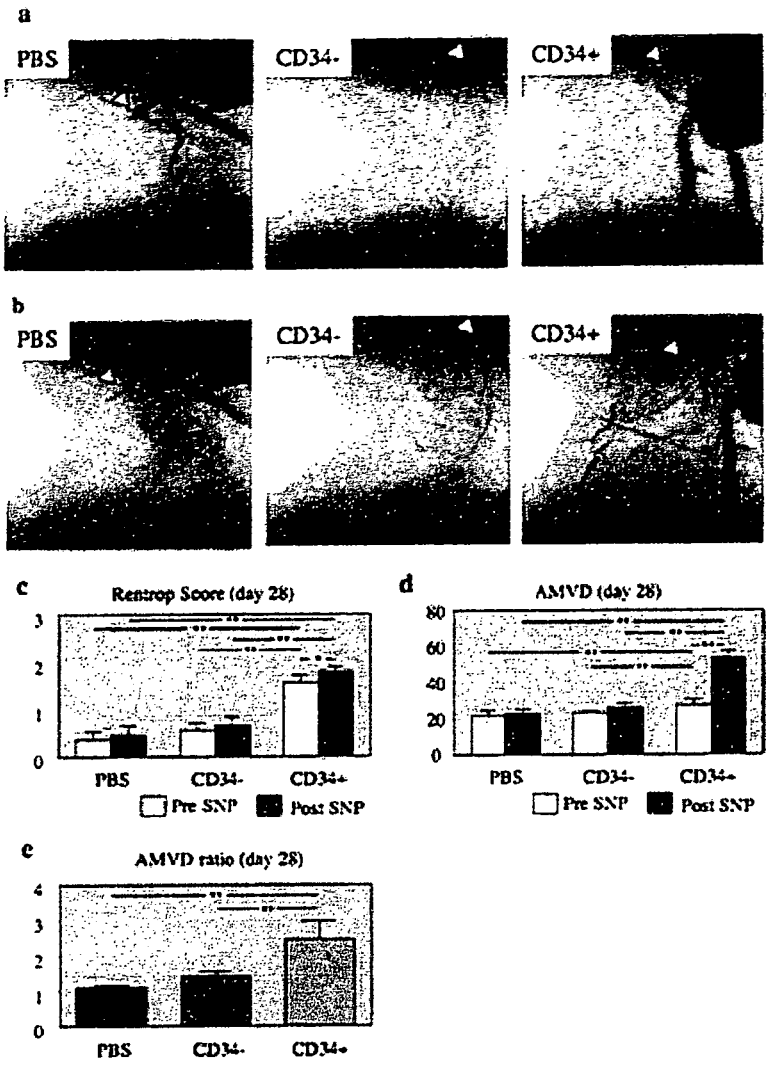

Figure 2. a, Representative microangiographic images pre SNP 28 days after PBS, CD34−, or CD34+ cell transplantation (7.0×7.0 mm). Collateral vessels were better developed in rat receiving CD34+ cells compared with rats receiving PBS and CD34− cells (scale bar, 100 μm). b, Representative microangiographic images post SNP at day 28 (7.0×7.0 mm). Augmentation of collateral microvessel development into distal portion of LAD area was further visualized in rat receiving CD34+ cells compared with rats receiving PBS and CD34− cells (scale bar, 100 μm). c, Rentrop score pre and post SNP at day 28 in each group. *$P<0.05$; **$P<0.01$. d, AMVD pre and post SNP at day 28 in each group. **$P<0.01$. e, AMVD ratio at day 28 in each group. **$P<0.01$.

pre SNP (post SNP, 53.2±3.8; pre SNP, 27.3±3.2, $P<0.05$). AMVD post SNP on day 28 was significantly greater in CD34+ cell group compared with CD34− cell and PBS groups (CD34+, 53.2±3.8; CD34−, 26.5±2.0, PBS, 23.0±2.0, $P<0.01$ for CD34+ versus CD34− and PBS) (Figure 2d). AMVD ratio on day 28 was also significantly greater in CD34+ cell group than either CD34− cell or PBS group (CD34+, 2.5±0.5; CD34−, 1.4±0.1, PBS, 1.1±0.1, $P<0.01$ for CD34+ versus CD34− or PBS). AMVD ratio on day 28 was similar in CD34− cell and PBS groups (Figure 2e).

These results indicate that AMVD analysis may be useful to quantify the effect of therapeutic neovascularization by CD34+ cell transplantation. Similarly as the Rentrop grade examination, AMVD assessment suggests contribution of CD34+ cell transplantation to improvement of collateral vessel function in response to SNP.

Histological Evaluation of Capillary Density

Histochemical staining for isolectin B4 was performed to identify capillaries in ischemic myocardium 4 weeks after cell transplantation (Figure 3a). Histological capillary density was significantly greater in CD34+ cell group than in CD34− cell and PBS groups. Histological capillary density in CD34− cell group was not significantly different from that in PBS group (CD34+, 711±15; CD34−, 365±23; PBS, 294±17/mm^2, $P<0.01$ for CD34+ versus CD34− and PBS) (Figure 3b).

Correlation Between SRM and Histological Assessments

To confirm whether AMVD is precise assessment of vascular development by CD34+ cell transplantation, we investigated correlation between AMVD and histological capillary density on day 28. AMVD pre SNP did not significantly correlate with histological capillary density ($R=0.16$, $P=0.42$), however AMVD post SNP closely correlated with histological capillary density ($R=0.82$, $P<0.0001$) (Figure 3c).

These results suggest that AMVD post SNP may be accurate and useful for precise evaluation of collateral and vascular formation following SCTx.

Discussion

Many investigators have demonstrated efficacy of various stem/progenitor cell transplantation against ischemic disease

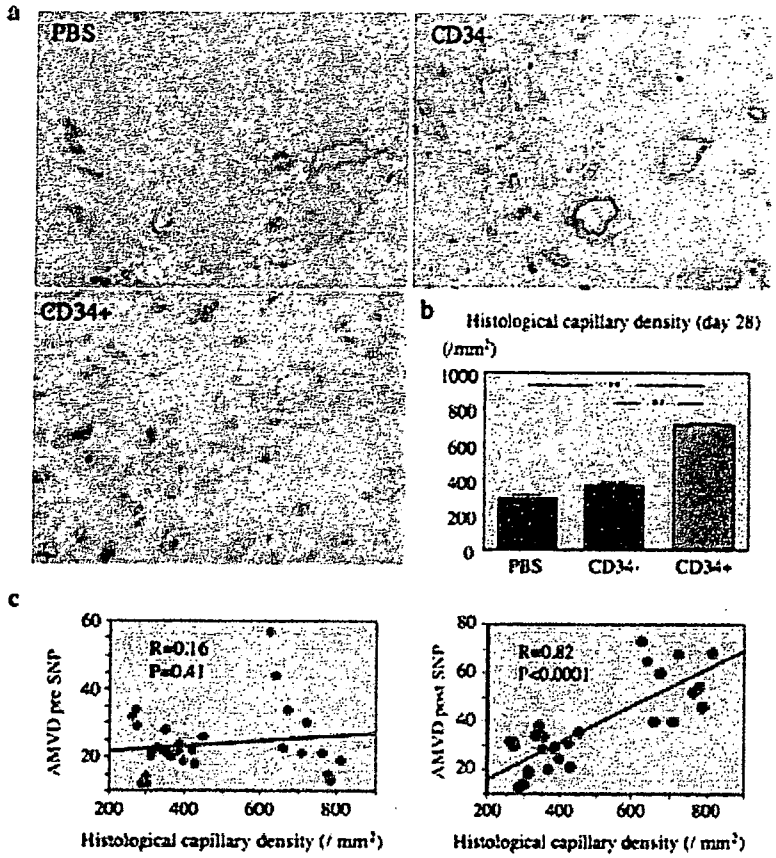

Figure 3. Histological and physiological evaluation of myocardial neovascularization after MI. a, Representative immunostaining for isolectin B4 in each group at day 28 (×200). b, Histological capillary density in rats receiving CD34+ cells, CD34− cells, or PBS at day 28. Ischemic neovascularization was significantly enhanced after CD34+ cell transplantation. $^{**}P<0.01$. c, Correlations of AMVD pre SNP or post SNP with histological capillary density 4weeks after the treatment. AMVD post SNP, but not pre SNP, closely correlated with histological capillary density.

such as MI and limb ischemia in vivo.[30,31] Although immunodeficient rats/mice provide enormous information about regenerative property of human stem/progenitor cells in the animal models of tissue ischemia, the vasculogenic/angiogenic effect of the human cells has been mainly evaluated by histological assessments because of technical limitation for physiological examinations in small animals.[15] Recently, Toyota et al[32] reported critical role of VEGF for coronary collateral growth by using micro CT. However, the micro CT can be performed only for postmortem examination, ie, not for fast beating hearts, and the spatial resolution of this method was 18 μm, which is 3 times larger than that in our novel SRM system and is not considered to be ideal for visualization of the collateral vessels.

In our SRM system, monochromatic SR is used as an x-ray source, and high speed and resolution imaging system, which has the potential to visualize blood vessels as small as 20 μm in diameter (spatial resolution: 6 μm), is also used. In the present study, we demonstrated usefulness of the SRM imaging to evaluate therapeutic neovascularization by cell-based therapy in small animals. Similarly as the previous reports,[4,7,8] histological and molecular examinations in this study confirmed endothelial differentiation and therapeutic efficacy of the transplanted CD34+ cells for augmentation of myocardial neovascularization. The SRM examination revealed that diameter of the collateral vessels was generally 20 to 120 μm, which is apparently invisible size in conventional angiography, and the collaterals were better visualized after SNP-induced vasodilatation than pre SNP. In comparison with postmortem studies such as histology, corrosion casts infusion and micro CT, it may be a great advantage of the SRM to elucidate physiology of the microvessels in response to vasoactive agents under the fast beating condition. To our knowledge, this is the first report demonstrating coronary microangiography under fast beating condition in both acute and chronic phases after MI and SCTx. Extent of collateral development was evaluated by conventional Rentrop score and novel assessment of AMVD. Although Rentrop score has been widely used in preclinical and clinical fields,[7] the examination has several limitations: (1) The scoring is semi-quantitative; (2) The system is to indirectly evaluate collateral development by grading collateral filling into the occluded coronary artery, and not to directly examine developed vascularization. Therefore, we assessed AMVD to quantitatively and directly evaluate blood vessel development as angiographic vessel density independent of blood flow in the occluded arteries. In the present study, both conventional and novel assessments revealed that collateral development and vascularization in ischemic myocardium was similar in all groups on day 5, but was significantly augmented in CD34+ cell group than other groups on day 28. Interestingly, the intergroup difference in AMVD was observed only post SNP, not pre SNP. Similarly, AMVD post SNP, not pre SNP, closely correlated with histological capillary density, which has been used for morphological evaluation of neovascularization in small animal studies. These results indicate accuracy and usefulness of AMVD post SNP for elucidating preserved vascular volume created by SCTx in fast beating

hearts of small animals, and also suggest that even in SRM with high imaging resolution, SNP infusion may be essential to avoid underestimation of the angiographic vascular density. The correlation between histological capillary density and AMVD post SNP proves the quality of AMVD to identify capillary vascular volume regenerated by SCTx. SNP infusion may increase the diameter of not only already visible vessels but also invisible capillaries (diameter <20 μm) pre SNP up to detectable size, thereby represents significant augmentation of blood perfusion in ischemic myocardium following CD34+ cell transplantation.

Present Limitations and Future Plans

The microangiographic imaging system requires a high shutter speed (short exposure time) to produce sharp and blur-free images of fast-moving hearts. In the current SRM system, the rotating disk X-ray shutter has been developed to produce X-ray pulses with the minimum pulse length of 0.1 ms, because even the beating heart is to remain almost motionless during the exposure time for ideal imaging. However, the exposure time was adjusted to around 2.0 ms in this experiment, because X-ray flux was not sufficient for the 0.1 ms shutter operation. A speed of the coronary arteries in rats is a few μm/ms at the end of diastole, ie, the movement of the arteries in 2.0 ms is several μm in the present system. On the other hand, the limiting spatial resolution of the image detector is approximately 6 μm, when digital images are acquired with a 1024×1024 pixel format, an input field of view of 4.5 mm×4.5 mm and pixel size of 4.5 μm. These facts indicate that the detector's spatial resolution is comparable to the motion blur amount in the present rat heart imaging, however there is still some room for improvement of the image quality. We are planning to develop a new X-ray optical system used for SR to increase the X-ray flux for the 0.1 ms shutter operation. Another limitation of the present study is that despite of the high quality of SRM for visualization of coronary arteries and the microvascular bed of fast beating hearts, we cannot take serial images in each individual at days 5 and 28, because they have to be examined ex vivo not in vivo. Future establishment of in vivo SRM imaging would be also warranted.

Conclusions

The present results indicate that the SRM may be useful to both morphologically and physiologically evaluate therapeutic neovascularization by SCTx in small animals. The novel imaging system may be not only an essential tool in future translational research of stem cell biology but also useful assessment of microvascular beds in small animal models of various diseases such as hypertension, diabetes mellitus, and cardiomyopathy. Further development of in vivo imaging system in future may lead to clinical application of the SRM, which is expected to be useful for assessment of microangiopathy, elucidation of therapeutic neovascularization, and determination of optimal treatment strategies in both preclinical and clinical trials.

Acknowledgments

We thank Yumiko Masukawa and Tomoko Itoh for their secretarial assistance. The synchrotron radiation experiments were performed at the BL28B2 in the SPring-8 with the approval of the Japan Synchrotron Radiation Research Institute (Proposal Nos. 2004B0339 and 2005A0590).

Sources of Funding

This work was supported by Health and Labor Sciences Research Grants (H14-trans-001, H17-trans-002) from Japanese Ministry of Health, Labor, and Welfare.

Disclosures

None.

References

1. Freedman SB, Isner JM. Therapeutic angiogenesis for coronary artery disease. *Ann Intern Med.* 2002;136:54–71.
2. Losordo DW, Vale PR, Hendel RC, Milliken CE, Fortuin FD, Cummings N, Schatz RA, Asahara T, Isner JM, Kuntz RE. Phase 1/2 placebo-controlled, double-blind, dose-escalating trial of myocardial vascular endothelial growth factor 2 gene transfer by catheter delivery in patients with chronic myocardial ischemia. *Circulation.* 2002;105:2012–2018.
3. Menasche P, Hagege AA, Scorsin M, Pouzet B, Desnos M, Duboc D, Schwartz K, Vilquin JT, Marolleau JP. Myoblast transplantation for heart failure. *Lancet.* 2001;357:279–280.
4. Kocher AA, Schuster MD, Szabolcs MJ, Takuma S, Burkhoff D, Wang J, Homma S, Edwards NM, Itescu S. Neovascularization of ischemic myocardium by human bone-marrow-derived angioblasts prevents cardiomyocyte apoptosis, reduces remodeling and improves cardiac function. *Nat Med.* 2001;7:430–436.
5. Asahara T, Murohara T, Sullivan A, Silver M, van der Zee R, Li T, Witzenbichler B, Schatteman G, Isner JM. Isolation of putative progenitor endothelial cells for angiogenesis. *Science.* 1997;275:964–967.
6. Asahara T, Masuda H, Takahashi T, Kalka C, Pastore C, Silver M, Kearne M, Magner M, Isner JM. Bone marrow origin of endothelial progenitor cells responsible for postnatal vasculogenesis in physiological and pathological neovascularization. *Circ Res.* 1999;85:221–228.
7. Kawamoto A, Tkebuchava T, Yamaguchi J, Nishimura H, Yoon YS, Milliken C, Uchida S, Masuo O, Iwaguro H, Ma H, Hanley A, Silver M, Kearney M, Losordo DW, Isner JM, Asahara T. Intramyocardial transplantation of autologous endothelial progenitor cells for therapeutic neovascularization of myocardial ischemia. *Circulation.* 2003;107:461–468.
8. Iwasaki H, Kawamoto A, Ishikawa M, Oyamada A, Nakamori S, Nishimura H, Sadamoto K, Horii M, Matsumoto T, Murasawa S, Shibata T, Suehiro S, Asahara T. Dose-dependent contribution of CD34-positive cell transplantation to concurrent vasculogenesis and cardiomyogenesis for functional regenerative recovery after myocardial infarction. *Circulation.* 2006;113:1311–1325.
9. Kawamoto A, Gwon HC, Iwaguro H, Yamaguchi JI, Uchida S, Masuda H, Silver M, Ma H, Kearney M, Isner JM, Asahara T. Therapeutic potential of ex vivo expanded endothelial progenitor cells for myocardial ischemia. *Circulation.* 2001;103:634–637.
10. Kemp PA, Gardiner SM, March JE, Rubin PC, Bennett T. Assessment of the effects of endothelin-1 and magnesium sulphate on regional blood flows in conscious rats, by the coloured microsphere reference technique. *Br J Pharmacol.* 1999;126:621–626.
11. Conrad MC, Anderson JL 3rd, Garrett JB Jr. Chronic collateral growth after femoral artery occlusion in the dog. *J Appl Physiol.* 1971;31:550–555.
12. Verheyen A, Vlaminckx E, Lauwers F, Van Den Broeck C, Wouters L. Serotonin-induced blood flow changes in the rat hindlegs after unilateral ligation of the femoral artery. Inhibition by the S2 receptor antagonist ketanserin. *Arch Int Pharmacodyn Ther.* 1984;270:280–298.
13. Orlandi C, Blackshear JL, Hollenberg NK. Specific increase in sensitivity to serotonin of the canine hindlimb collateral arterial tree via the 5-hydroxytryptamine-2 receptor. *Microvasc Res.* 1986;32:121–130.
14. Takeshita S, Zheng LP, Brogi E, Kearney M, Pu LQ, Bunting S, Ferrara N, Symes JF, Isner JM. Therapeutic angiogenesis. A single intraarterial bolus of vascular endothelial growth factor augments revascularization in a rabbit ischemic hind limb model. *J Clin Invest.* 1994;93:662–670.
15. Mori H, Hyodo K, Tobita K, Chujo M, Shinozaki Y, Sugishita Y, Ando M. Visualization of penetrating transmural arteries in situ by monochromatic synchrotron radiation. *Circulation.* 1994;89:863–871.
16. Mori H, Hyodo K, Tanaka E, Uddin-Mohammed M, Yamakawa A, Shinozaki Y, Nakazawa H, Tanaka Y, Sekka T, Iwata Y, Handa S,

Umetani K, Ueki H, Yokoyama T, Tanioka K, Kubota M, Hosaka H, Ishikawa N, Ando M. Small-vessel radiography in situ with monochromatic synchrotron radiation. *Radiology*. 1996;201:173–177.

17. White FC, Carroll SM, Magnet A, Bloor CM. Coronary collateral development in swine after coronary artery occlusion. *Circ Res*. 1992;71:1490–1500.
18. Unger EF, Banai S, Shou M, Lazarous DF, Jaklitsch MT, Scheinowitz M, Correa R, Klingbeil C, Epstein SE. Basic fibroblast growth factor enhances myocardial collateral flow in a canine model. *Am J Physiol*. 1994;266:H1588–1595.
19. Takeshita S, Rossow ST, Kearney M, Zheng LP, Bauters C, Bunting S, Ferrara N, Symes JF, Isner JM. Time course of increased cellular proliferation in collateral arteries after administration of vascular endothelial growth factor in a rabbit model of lower limb vascular insufficiency. *Am J Pathol*. 1995;147:1649–1660.
20. Rubenstein E, Hofstadter R, Zeman HD, Thompson AC, Otis JN, Brown GS, Giacomini JC, Gordon HJ, Kernoff RS, Harrison DC, et al. Transvenous coronary angiography in humans using synchrotron radiation. *Proc Natl Acad Sci U S A*. 1986;83:9724–9728.
21. Mori H, Tanaka E, Hyodo K, Uddin Mohammed M, Sekka T, Ito K, Shinozaki Y, Tanaka A, Nakazawa H, Abe S, Handa S, Kubota M, Tanioka K, Umetani K, Ando M. Synchrotron microangiography reveals configurational changes and to-and-fro flow in intramyocardial vessels. *Am J Physiol*. 1999;276:H429–H437.
22. Takeshita S, Isshiki T, Mori H, Tanaka E, Eto K, Miyazawa Y, Tanaka A, Shinozaki Y, Hyodo K, Ando M, Kubota M, Tanioka K, Umetani K, Ochiai M, Sato T, Miyashita H. Use of synchrotron radiation microangiography to assess development of small collateral arteries in a rat model of hindlimb ischemia. *Circulation*. 1997;95:805–808.
23. Tanaka E, Tanaka A, Sekka T, Shinozaki Y, Hyodo K, Umetani K, Mori H. Digitized cerebral synchrotron radiation angiography: quantitative evaluation of the canine circle of Willis and its large and small branches. *Am J Neuroradiol*. 1999;20:801–806.
24. Sekka T, Volchikhina SA, Tanaka A, Hasegawa M, Tanaka Y, Ohtani Y, Tajima T, Makuuchi H, Tanaka E, Iwata Y, Sato S, Hyodo K, Ando M, Umetani K, Kubota M, Tanioka K, Mori H. Visualization, quantification and therapeutic evaluation of angiogenic vessels in cancer by synchrotron microangiography. *J Synchrotron Radiat*. 2000;7:361–367.
25. Kidoguchi K, Tamaki M, Mizobe T, Koyama J, Kondoh T, Kohmura E, Sakurai T, Yokono K, Umetani K. In vivo X-ray angiography in the mouse brain using synchrotron radiation. *Stroke*. 2006;37:1856–1861.
26. Gaipa G, Dassi M, Perseghin P, Venturi N, Corti P, Bonanomi S, Balduzzi A, Longoni D, Uderzo C, Biondi A, Masera G, Parini R, Bertagnolio B, Uziel G, Peters C, Rovelli A. Allogeneic bone marrow stem cell transplantation following CD34+ immunomagnetic enrichment in patients with inherited metabolic storage diseases. *Bone Marrow Transplant*. 2003;31:857–860.
27. Beaussier M, Mouren S, Souktani R, Arthaud M, Massias L, Vicaut E, Lienhart A, Coriat P. Role of nitric oxide and cyclooxygenase pathways in the coronary vascular effects of halothane, isoflurane and desflurane in red blood cell-perfused isolated rabbit hearts. *Br J Anaesth*. 2002;88:399–407.
28. Heitzer T, Baldus S, von Kodolitsch Y, Rudolph V, Meinertz T. Systemic endothelial dysfunction as an early predictor of adverse outcome in heart failure. *Arterioscler Thromb Vasc Biol*. 2005;25:1174–1179.
29. Becker A, Reith A, Napiwotzki J, Kadenbach B. A quantitative method of determining initial amounts of DNA by polymerase chain reaction cycle titration using digital imaging and a novel DNA stain. *Anal Biochem*. 1996;237:204–207.
30. Orlic D, Kajstura J, Chimenti S, Jakoniuk I, Anderson SM, Li B, Pickel J, McKay R, Nadal-Ginard B, Bodine DM, Leri A, Anversa P. Bone marrow cells regenerate infarcted myocardium. *Nature*. 2001;410:701–705.
31. Jackson KA, Majka SM, Wang H, Pocius J, Hartley CJ, Majesky MW, Entman ML, Michael LH, Hirschi KK, Goodell MA. Regeneration of ischemic cardiac muscle and vascular endothelium by adult stem cells. *J Clin Invest*. 2001;107:1395–1402.
32. Toyota E, Warltier DC, Brock T, Ritman E, Kolz C, O'Malley P, Rocic P, Focardi M, Chilian WM. Vascular endothelial growth factor is required for coronary collateral growth in the rat. *Circulation*. 2005;112:2108–2113.

Ann Nucl Med (2007) 21:189–196
DOI 10.1007/s12149-007-0015-1

ORIGINAL ARTICLE

Diagnostic performance of CT, PET, side-by-side, and fused image interpretations for restaging of non-Hodgkin lymphoma

Munenobu Nogami · Yuji Nakamoto · Setsu Sakamoto
Kazuto Fukushima · Tomohisa Okada · Tsuneo Saga
Tatsuya Higashi · Michio Senda · Toshimitsu Matsui
Kazuro Sugimura

Received: 13 November 2006 / Accepted: 2 February 2007

Abstract
Objective The purpose of this study was to compare the diagnostic performance of positron emission tomography (PET) alone, computed tomography (CT) alone, side-by-side reading, and fused images for restaging or follow-up of patients with malignant lymphoma.
Methods Fifty patients with histologically confirmed non-Hodgkin lymphoma underwent an ^{18}fluoro-2-deoxyglucose (FDG)-PET scan, followed by a CT scan. CT alone, PET alone, side-by-side reading, and fused images were interpreted separately and visually using a five-point grading scale for the following eight regions: cervical, supraclavicular, axillary, mediastinal, para-aortic to iliac, mesenteric, inguinal, and extra-nodal. Diagnostic accuracy was compared on the basis of the final diagnoses determined by histological confirmation and/or clinical course.
Results For all regions combined, the interpretation of PET alone (sensitivity = 86.1%, specificity = 99.4%, accuracy = 91.0%), side-by-side reading (96.0%, 99.4%, 98.9%), and fused images (98.0%, 99.4%, 99.2%) yielded significantly higher diagnostic performance than that of CT alone (59.4%, 96.1%, 91.0%; $P < 0.001$). The cervical, supraclavicular, and extra-nodal regions were more accurately diagnosed with PET ($P < 0.05$), whereas the para-aortic to iliac regions were diagnosed more accurately with side-by-side reading and fused images than with CT alone or PET alone ($P < 0.05$).
Conclusions Although fused images are clinically valuable, side-by-side reading showed equivalent performance, whereas the interpretation of PET alone yielded reasonably high diagnostic performance for restaging or follow-up of patients with malignant lymphoma.

Keywords CT · PET · Lymphoma · Image fusion

M. Nogami (✉) · S. Sakamoto · K. Sugimura
Department of Radiology, Kobe University Graduate School of Medicine, 7-5-2 Kusunoki-cho, Chuo-ku, Kobe 650-0017, Japan
e-mail: aznogami@med.kobe-u.ac.jp

Y. Nakamoto · T. Saga · T. Higashi
Department of Diagnostic Imaging and Nuclear Medicine, Kyoto University Graduate School of Medicine, Kyoto, Japan

K. Fukushima
Department of Nuclear Medicine, National Cardiovascular Center, Osaka, Japan

T. Okada
Department of Radiology, Kobe City General Hospital, Kobe, Japan

M. Senda
Department of Image-Based Medicine, Institute of Biomedical Research and Innovation, Kobe, Japan

T. Matsui
Division of Hematology/Oncology, Department of Medicine, Kobe University School of Medicine, Kobe, Japan

Introduction

Computed tomography (CT) has been one of the main diagnostic modalities for the staging, restaging, and follow-up of patients with lymphoma. CT can provide precise anatomic information and depict abnormal structures and abnormal contrast enhancement resulting from pathological changes of lesions [1–3]. Because interpretations using CT are made mainly based on size criteria [4], we can neither detect pathological lesions in normal-

sized lymph nodes nor differentiate nodes enlarged by other causes. Another drawback of CT for patients with lymphoma is the difficulty of detecting tumors in cases of diminished contrast with the surrounding tissues. These disadvantages of CT result in a reduced sensitivity for lesion detection [4, 5].

Rather than morphological information, positron emission tomography (PET) using fluorine-18-fluoro-2-deoxy-D-glucose (FDG) provides metabolic information on glucose uptake and is useful for the management of patients with lymphoma [4, 6–13]. The main disadvantages of PET tumor imaging are low contrast, low resolution, and less effective visualization of anatomic landmarks. These drawbacks make it difficult to accurately localize lesions with pathological FDG uptake [5, 14], so that it is also usually necessary to refer to morphological imaging such as CT to interpret PET images (side-by-side reading) [1].

To complement morphological information, an inline PET/CT system has been developed with its clinical viability confirmed in several reports [1, 5, 14, 15]. This system is advantageous when lesions are adjacent to structures which cannot be conclusively assessed through interpretations arrived at by means of by PET alone or CT alone [15].

In spite of the known advantages of fused images provided by a combined PET/CT scanner for the assessment of malignant lymphoma [3, 16–18], not all institutes have access to this new technology because of its higher cost. This has resulted in a continuing demand for investigations of the clinical feasibility of software-based manual fusion techniques. Image fusion can now actually be achieved using software, and reportedly high diagnostic accuracy was obtained even with this approach [19].

The purpose of our study was to compare the diagnostic performance of CT alone, PET alone, side-by-side reading, and manually fused images for patients with lymphoma.

Materials and methods

Subjects

Fifty patients (30 men and 20 women; mean age 53.8 years; range 20–76 years) with histologically confirmed non-Hodgkin lymphoma underwent an FDG-PET scan followed by a CT scan at our institute between June 2003 and November 2004. Patients with diabetes mellitus were excluded from our study to avoid false-negative results on PET resulting from an elevated plasma glucose level [20]. The scans were performed on 24 patients for restaging and on 26 for follow-up. The scans for restaging were for the evaluation of therapeutic effect after completion of chemotherapy or chemo radiotherapy, and scans for follow-up were used for checking for recurrence after a complete response had been achieved. The duration between restaging examination and completion of therapy ranged from 3 to 10 weeks (mean 4.2 weeks), and that between follow-up examination and confirmation of complete response ranged from 12 to 26 weeks (mean 15.3 weeks). The World Health Organization histological classifications of the recruited patients with non-Hodgkin lymphoma were B-cell lymphoma ($n = 44$) and T-cell lymphoma ($n = 6$). Written informed consent was obtained from all patients, and the ethics committee of our institute approved this study.

PET examinations

All patients fasted for at least 4 h before the examination and received 111–148 MBq (3–4 mCi) of FDG. Plasma glucose levels were monitored just before the intravenous administration of FDG (range 72–133 mg/dl, average 92 mg/dl). Patients were urged to void 50-min postinjection, after which they were positioned on a 200 × 60 × 5 cm large vacuum cushion (ESFORM; Engineering System, Matsumoto, Japan), which has been widely used for positioning patients for radiation therapy. The cushion was placed on the bed of a PET scanner, and the patients were positioned on top with their arms up over the head as previously described [19]. With a felt-tip pen, a median line from the navel to the sternum level was drawn on the skin, as well as bilateral horizontal longitudinal lines, and a transverse line on the upper thigh indicating the starting point for scanning.

Positron emission tomography studies were performed with either an ECAT Exact 47 or an ECAT Exact HR+ PET Camera (Siemens/CTI, Knoxville, TN, USA). These devices simultaneously acquire 47 planes over a 16.2-cm (ECAT Exact 47) or 63 planes over a 15.5-cm (ECAT Exact HR+) axial field of view. After placement of the patients as described earlier, a static emission scan was performed with 2–3 min of acquisition for each bed position and covering an area from the upper thigh to the meatus of the ear. Next, a transmission scan using a $^{68}Ge/^{68}Ga$ rod source was performed over the same area for 2 min per bed position. All acquisitions were three dimensional. Attenuation-corrected images were obtained by using an ordered-subsets expectation maximization iterative reconstruction algorithm (four iterations, eight subsets). Delayed PET scan was neither performed nor interpreted in this study because delayed scan for patients with lymphoma is not routinely performed in our institute.

CT examinations

After completion of the PET scan, patients were urged to void again to obtain a consistent bladder shape and reduce radiation exposure. They were then moved to the CT room, where they were repositioned on the same molded vacuum cushion and with reference to the same median and bilateral surface lines that were drawn before the PET scan. The CT device was a multidetector row CT scanner (Acquilion; Toshiba Medical Systems, Tokyo, Japan) with four detectors. The following technical parameters were used for CT scanning: 120 kV peak energy, and 200–450 mA electric current with automated radiation exposure control, helical pitch of 5.5 mm (high-speed mode), 3-mm collimation, and 5-mm reconstruction thickness. During the 20–30-s scan, the patients were requested to perform shallow breathing. The CT examinations were performed with (n = 47) or without (n = 3) contrast material, and all the contrast-enhanced CTs were acquired during the equilibrium phase, i.e. 80–90 s after intravenous injection of 100 ml of Iohexol (Omnipaque 300; Daiichi Pharmaceutical, Tokyo, Japan). The interval between PET and CT scans was less than 1 h in all patients.

Image fusion

Both CT and PET data sets were transferred to a SUN workstation (ULTRA60; SUN Microsystems, Mountain View, CA, USA). To obtain fused images of CT and PET, the PET images, which had been enlarged with a multiple zoom factor in order to match the field of view of CT images (50 cm), were interpolated with software (Dr.View; Asahikasei-Joho Systems, Tokyo, Japan) into a matrix size of 512 × 512 with 5-mm intervals. The slice showing the lower margin of the urinary bladder was then identified on both CT and modified PET images, and the PET images were shifted cranio-caudally to match the CT images. In this manner, by using the two slices showing the lower margin of the bladder, the two sets of images were merged on a pixel-to-pixel basis.

Image analysis

First, two board-certified radiologists (TO, 14 years of experience; YN, 13 years of experience) read the CT images without access to any clinical information. Both size and shape criteria were used for CT interpretation, with round lymph nodes with a short axis longer than 1 cm being considered abnormal in comparison with lymph nodes that were flat and/or had a short axis less than 1 cm in length. After interpretation of CT images only, two radiologists (YN, 13 years of experience; SS, 12 years of experience), who were also board-certified nuclear medicine physicians, interpreted the fused images. In order to avoid interpretation bias, PET images alone were read by two other board-certified nuclear medicine physicians (TS, 22 years of experience; TH, 15 years of experience) without access to any other information, including CT image interpretations. Regions with focally increased tracer uptake were interpreted as abnormal. Because the purpose of the study was to assess the visual interpretation of each modality, semi-quantitative parameters of FDG uptake, such as a standardized uptake value, were not used. For side-by-side reading, PET and CT images were juxtaposed and interpreted by two different board-certified radiologists (TO, 14 years of experience; MN, 7 years of experience).

All image interpretations were performed with the aid of a workstation that provided the appropriate intensity for PET and the optimal density level for CT. To assess the diagnostic capability of each type of interpretation, findings were compared on the basis of the following anatomic regions: cervical, supraclavicular, axillary, mediastinal, para-aortic to iliac, mesenteric, inguinal, and extranodal. The number of lesions in each region was not counted. Interpretations of the images were scored on a five-point grading scale (0 = definitely negative, 1 = probably negative, 2 = equivocal, 3 = probably positive, 4 = definitely positive) by consensus of the two readers. A lesion in the extranodal region was identified and interpreted separately for each interpretation and was scored "0" when no corresponding lesion was detected by the other interpretations. Regions with a score of 3 or 4 were interpreted as positive, and those with grade 0 through 2 were considered negative for each interpretation.

Standard reference

Final diagnosis was determined by histological confirmation and/or clinical follow-up of at least 12 months (mean duration 24.1 months; range 12.1–36.2 months). Assessment of five regions in five patients was confirmed histologically by means of biopsy. The remaining regions without histological confirmation were evaluated by means of clinical follow-up consisting of several imaging modalities such as follow-up PET study (n = 32), magnetic resonance imaging (MRI) (n = 2), and follow-up CT (n = 48). Fused images, obtained with the same procedure as described before, were included in the follow-up studies (n = 32). Final diagnosis of the regions arrived at with the various imaging modalities was defined as follows: when the region was diagnosed as positive with every method, a finding of enlargement of the lesion and/or residual (or increased) accumulation re-

gardless of therapy, or a finding of a decrease in size and/or accumulation after therapy during the follow-up study was regarded as true positive, whereas a finding of a decrease in size and/or accumulation without therapy was considered false positive. When the region was diagnosed as negative with every method, a finding of a lack of enlargement and/or accumulation in the region regardless of therapy was considered as true negative, and a finding of an increase in size and/or accumulation regardless of therapy was judged to be false negative.

Statistical analysis

To determine the diagnostic confidence of the interpretations, true-positive regions which were scored as "4" by every interpretative method were statistically compared by means of the chi-square test.

To assess the individual diagnostic performance of each of the interpretation modalities, sensitivity, specificity, and accuracy of CT alone, PET alone, side-by-side reading, and fused images were each assessed on the basis of the final diagnoses. To compare the diagnostic performance of each modality thus assessed, the receiver operating characteristic analysis followed by McNemar's test was applied.

We used commercially available software (Statview, version 5.0, SAS Institute, Cary, NC, USA and Statmate III, HALLoGRAM Publishing, Aurora, CO, USA) for statistical analysis. For all statistical analyses, a P value of less than 0.05 was considered to indicate a statistically significant difference.

Results

The number of involved regions was 100 in 25 patients. The scores determined by each of the interpretation modalities for the true-positive regions are shown in Table 1. The number of true-positive regions which were scored as "4" was 47 (47%) for CT alone, 68 (68%) for PET alone, 84 (84%) for side-by-side reading, and 91 (91%) for fused image interpretation. The differences in scores between the interpretations of CT alone and the other modalities were all statistically significant by the chi-square test ($P < 0.001$). The difference between the interpretations of PET alone and fused images was also statistically significant ($P < 0.01$). There was no significant difference between the interpretations of side-by-side and fused images.

Table 1 Distribution of scores for true-positive regions determined with each of the modalities ($n = 100$)

Score	CT alone	PET alone	Side-by-side	Fused image
0	13 (13%)	4 (4%)	2 (2%)	1 (1%)
1	15 (15%)	2 (2%)	0 (0%)	0 (0%)
2	12 (12%)	8 (8%)	1 (1%)	0 (0%)
3	13 (13%)	18 (18%)	13 (13%)	8 (8%)
4	47 (47%)	68 (68%)	84 (84%)	91 (91%)

PET positron emission tomography, *CT* computed tomography

The diagnostic performance and area under the curve for each method on a per-region basis are summarized in Table 2. For the overall regions, the interpretation of PET images alone (sensitivity = 83.9%, specificity = 99.5%, accuracy = 91.9%, area under the curve = 0.959), side-by-side reading (94.6%, 99.3%, 98.8%, 0.981), and fused images (98.2%, 99.3%, 99.2%, 0.991) showed higher diagnostic performance than did that of CT images alone (48.2%, 96.4%, 91.9%, 0.791) as determined by McNemar's test ($P < 0.001$) (Table 3, Fig. 1).

For the cervical regions, CT showed the lowest diagnostic value by a significant margin ($P < 0.01$). For the para-aortic to iliac region, there was no significant difference between the diagnostic performance of CT and PET, and that of CT was significantly poorer than the performance of side-by-side reading and fused images ($P < 0.01$) (Table 3).

Fifteen extranodal regions were found in nine patients of our study population. These extranodal regions

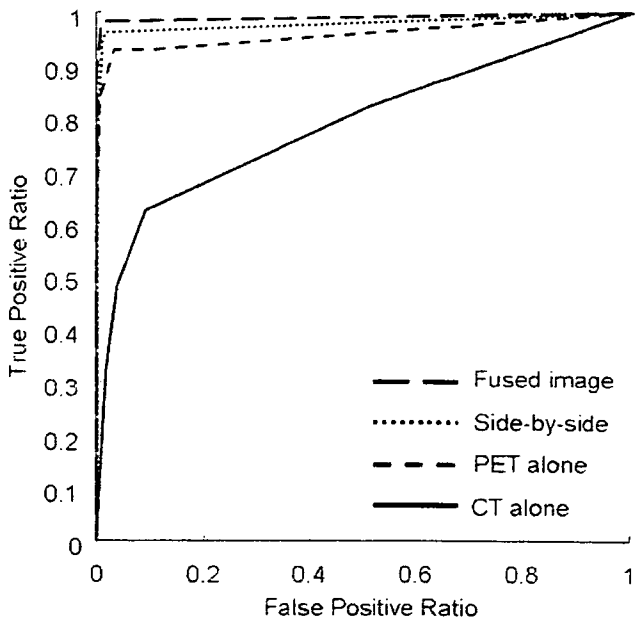

Fig. 1 Receiver operating characteristic analysis curves for the overall regions. The diagnostic performance of positron emission tomography (PET)-alone interpretation, side-by-side reading, and fused image interpretation was significantly better than that of computed tomography (CT)-alone interpretation ($P < 0.001$). There was no significant difference in the diagnostic efficacy among PET-alone interpretation, side-by-side reading, and fused image interpretation for the overall regions

Table 2 Diagnostic performance of the methodologies assessed by region-based analysis

Region	CT only				PET only				Side-by-side reading				Fused image			
	SS	SP	AC	Az	SS	SP	AC	Az	SS	SP	AC	Az	SS	SP	AC	Az
Overall (n = 100)	48.2	96.4	91.9	0.791	83.9	99.5	91.9	0.959	94.6	99.3	98.8	0.981	98.2	99.3	99.8	0.991
Cervical (n = 19)	50.0	94.4	90.0	0.791	90.0	100.0	90.0	0.999	100.0	100.0	100.0	0.000	100.0	100.0	100.0	1.00
Supraclavicular (n = 11)	33.3	99.0	97.0	0.747	66.7	100.0	97.0	1.00	66.7	100.0	99.0	0.000	100.0	100.0	100.0	1.00
Axillary (n = 19)	40.0	100.0	94.0	0.950	80.0	98.9	94.0	0.996	100.0	98.9	99.0	0.999	100.0	100.0	99.0	0.999
Mediastinal (n = 6)	75.0	97.8	100.0	1.00	100.0	100.0	100.0	0.978	100.0	100.0	100.0	0.000	100.0	100.0	100.0	1.00
Para-aortic to iliac (n = 12)	40.0	96.7	91.0	0.806	80.0	100.0	91.0	0.946	100.0	98.9	91.0	0.806	100.0	98.9	99.0	0.999
Mesenteric (n = 4)	100.0	95.9	96.0	0.980	100.0	100.0	96.0	1.00	100.0	100.0	100.0	0.000	100.0	100.0	100.0	1.00
Inguinal (n = 14)	75.0	95.2	96.0	0.854	75.0	100.0	96.0	0.818	87.5	100.0	98.0	0.938	100.0	100.0	100.0	1.00
Extranodal (n = 15)	30.0	87.5	77.6	0.573	90.0	95.8	94.8	0.927	90.0	95.8	94.8	0.933	90.0	95.8	94.8	0.940

SS sensitivity, *SP* specificity, *AC* accuracy, *AZ* area under the curve

Table 3 Comparison of diagnostic performance of the methodologies by means of receiver operating characteristic analysis

	CT vs. PET	CT vs. S-by-S	CT vs. fused	PET vs. S-by-S	PET vs. fused	S-by-S vs. fused
Overall	$P < 0.001$	$P < 0.001$	$P < 0.001$	NS	NS	NS
Cervical	$P < 0.01$	$P < 0.01$	$P < 0.01$	NS	NS	NS
Supraclavicular	NS	NS	NS	NS	NS	NS
Axillary	NS	NS	NS	NS	NS	NS
Mediastinal	NS	NS	NS	NS	NS	NS
Para-aortic to iliac	NS	$P < 0.01$	$P < 0.01$	NS	NS	NS
Mesenteric	NS	NS	NS	NS	NS	NS
Inguinal	NS	NS	NS	NS	NS	NS
Extranodal	$P < 0.001$	$P < 0.001$	$P < 0.001$	NS	NS	NS

NS not statistically significant, *S-by-S* side-by-side reading, *Fused* fused image

comprised spleen, thyroid, nasopharynx (n = 2), spine, rib (n = 2), pelvic bone, lung (n = 3), peritoneum, colon, uterus, and brain. In these regions, the diagnostic performance of CT alone was significantly poorer than that of PET alone, side-by-side reading, and fused images ($P < 0.001$). On the other hand, the latter three modalities showed no significant differences in the assessment of the extranodal region (Table 3).

Discussion

Our study indicates that the overall diagnostic performance of PET alone, side-by-side reading, and fused image interpretation do not differ significantly for restaging or follow-up of patients with malignant lymphoma but was significantly superior to interpretation on the basis of CT alone.

On interpretation of CT alone, the detection of lesions depends on the capability of distinguishing abnormal structures from surrounding normal organs. Even when contrast material was administered to 47 of the 50 patients (94%) in our study, the overall sensitivity of interpretation with CT alone was only 48.2%, and was especially low in the extranodal region (30.0%). Figure 2 shows an example of a patient with extranodal involvement in the nasopharynx, which was overlooked in CT alone. Schaefer et al. [3] reported similar results consistent with our data regarding poorer diagnostic performance for extranodal involvement by the interpretation of contrast-enhanced CT [3].

In the nodal region, the interpretation of CT alone mainly depends on size criteria to determine whether lesions are pathological [4, 7, 16, 21], so that normal- or borderline-sized lymph nodes with malignancy could be diagnosed as normal. This is especially true for the

restaging of lymphomas after therapy and residual enlarged nodes without viability, which can be seen in up to 80% of patients with Hodgkin lymphoma and in up to 40% of non-Hodgkin lymphoma patients [16]. The region-based analysis in our study demonstrated that the diagnostic performance of CT-alone interpretation in the cervical regions was significantly lower than that of the other interpretation modalities. Because normal- or borderline-sized lymph nodes without malignancy are commonly seen in these regions, it is hard to differentiate malignant from benign lesions by depending on size criteria as well as to show abnormalities that are surrounded by normal tissues such as muscles and vessels (Fig. 3).

An inline PET/CT scanner has been developed to overcome the lack of anatomical information which has been a disadvantage of PET, and is reportedly beneficial for the assessment of patients with lymphoma [1, 5, 14, 15, 18]. Restaging of three patients in our study was performed correctly by fused image interpretation, but interpreted as false negative by PET alone. Figure 4 shows one of these cases. For the assessment of interpretation by PET alone, the detection of abnormality depends on differentiation between physiological and pathological uptake. It is therefore possible that abnormal uptake was overlooked when it was located adjacent to physiological uptake such as the heart in the mediastinal region, the ureter in the para-aortic to iliac region, the intestinal tract in the mesenteric or inguinal regions and the brain, liver, kidney, and bladder in the extranodal region. Moreover, far fewer true-positive regions were scored as "4" by PET alone than by fused image interpretation. As Tatsumi et al. [22] showed, a fused image has an advantage over separate PET and CT interpretation in terms of lesion detection and diagnostic confidence. For those reasons, anatomical information is required to avoid false-negative findings by PET-alone interpretation and to enhance the diagnostic confidence for the assessment of lymphoma.

On the other hand, the diagnostic performance of PET alone for the overall regions as assessed by region-based analysis was much better than expected and showed no statistical difference when compared with that of side-by-side reading or fused image interpretation. For restaging or follow-up of patients with lymphoma, precise anatomical information is not always essential when compared with that for patients with other malignancies such as lung cancer, because anatomical information in lymphoma is used to distinguish nodal from extranodal and supradiaphragmatic from infradiaphragmatic [3, 23]. The interpretation of PET alone may therefore be sufficient for the assessment of patients with lymphoma for restaging or follow-up. In other words, the diagnostic performance of interpretation modalities that includes PET images, regardless of whether they are side-by-side reading or fused image interpretations, is not statistically different and is sufficient for the management of patients with lymphoma after therapy.

Although the diagnostic performance of fused image assessment was superior in terms of both overall and individual regions to that of side-by-side reading, the advantage of the former was so small that no statistically significant difference was observed in our study. Reinartz et al. [15] showed similar results for a comparison of the diagnostic performance between side-by-side reading and reading with a combined PET/CT scanner. They concluded that the diagnostic performance of side-by-side reading was so outstanding that the additional information obtained with a fused image was small but substantial in certain situations.

One extranodal region in our study population was misdiagnosed as false negative even by fused image interpretation. In this patient, brain infiltration was detected on MRI after PET examination, but overlooked by all the other interpretation modalities including CT and PET. This is because the use of latter two modalities is problematic for the detection of brain tumors because of the low-density resolution on CT and physiological uptake of the brain on PET [24].

By adopting our fusion technique using a fixation device, fused images were easily acquired without the need for a dedicated PET/CT system and requiring only a little extra time [19]. In addition, the fused images thus obtained yielded small displacement between separately acquired CT and PET images, thus resulting in a better diagnostic performance. We believe that our fused PET and CT data achieved a diagnostic performance equivalent to, but slightly different from, that of an inline PET/CT system. For this reason, further investigations comparing the diagnostic performance of fused images acquired by our software-based approach and of PET/CT are warranted.

Our study has certain limitations. First, a pathological diagnosis is for ethical reasons usually not possible for all the detected lesions and abnormalities; therefore we had to refer to a final diagnosis determined by histological confirmation and/or clinical follow-up for at least 12 months. These final diagnoses were then used as a reference standard for comparisons among the diagnostic performance of CT alone, PET alone, side-by-side reading, and fused images. Moreover, 20 of the 50 patients were followed up with morphological imaging modalities alone. Second, because patients with lymphomas of various histological classifications were included in our study population, the uptake intensity of lesions

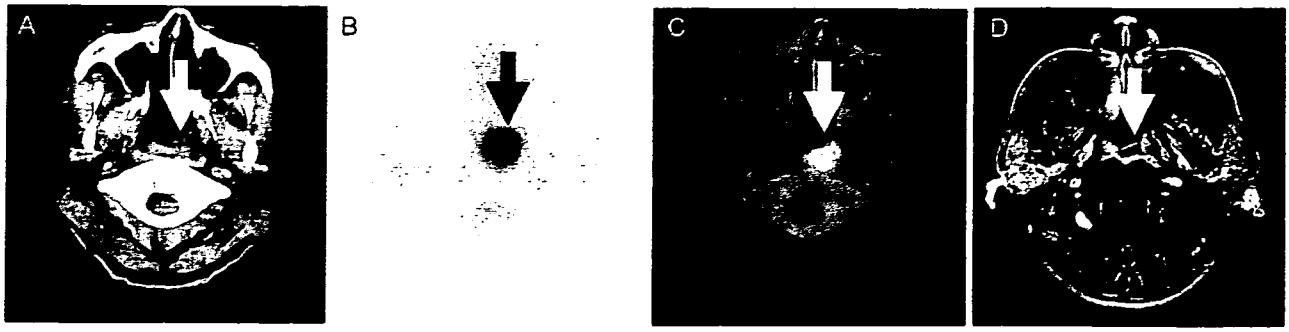

Fig. 2 A 56-year-old man with nasopharyngeal (extranodal) involvement of testicular diffuse large B-cell lymphoma. Focal uptake around the nasopharynx was found on the PET image (**b**), but it was difficult to diagnose this abnormality on the corresponding CT image (**a**). MR imaging (fat-suppressed, gadolinium-enhanced, T1-weighted image) showed an intermediate intense lesion in the nasopharyngeal region (**d**). This lesion was confirmed by biopsy

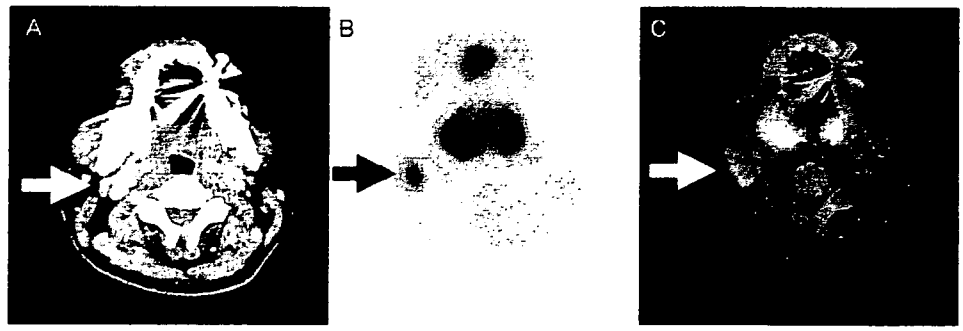

Fig. 3 A 44-year-old man with cervical involvement of orbit B-cell lymphoma after chemotherapy 1 year previously. PET and CT scans showed recurrence. Focal uptake in the right cervical region was found on the PET image (**b**), but it was difficult to read the lesion as positive on the corresponding CT image (**a**). This lesion had disappeared on the follow-up PET scan after chemotherapy

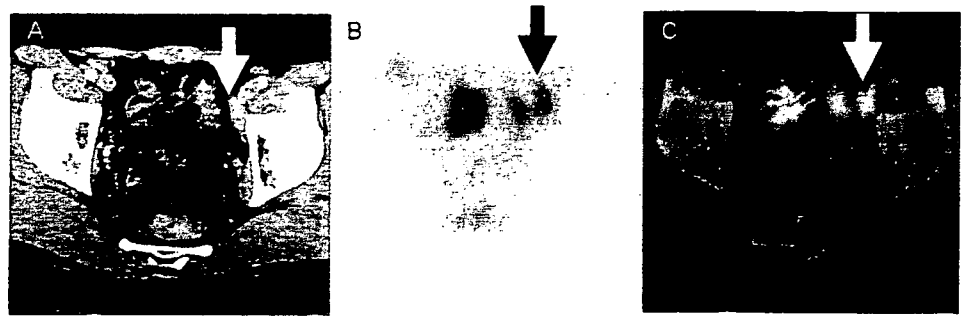

Fig. 4 A 56-year-old man with iliac lymph node involvement of orbit marginal zone B-cell lymphoma. Intermediate uptake in the left iliac region was found on the PET image, but it was difficult to differentiate from physiological uptake of intestine. Moreover, the lesion was overlooked on the CT image (**a**), probably because it was considered to be a vessel. Involvement was confirmed by biopsy

could vary depending on the histological subtype. Therefore, a lymphoma subtype with low FDG uptake such as mucosa-associated lymphoid tissue lymphoma (extranodal marginal zone B-cell lymphoma) [25, 26] is likely to affect the diagnostic performance of modalities using PET imaging.

In conclusion, the most accurate diagnosis was obtained by interpreting fused images, followed by side-by-side reading and interpreting PET alone. Although fused images are clinically the most valuable, the diagnostic performance of side-by-side reading was found to be equivalent when the aim of the examination is restaging

or follow-up. The area-based diagnostic accuracy of PET-alone interpretation was also reasonably high for patients with lymphoma when compared with that of combined image interpretation.

References

1. Messa C, Bettinardi V, Picchio M, Pelosi E, Landoni C, Gianolli L, et al. PET/CT in diagnostic oncology. Q J Nucl Med Mol Imaging 2004;48(2):66–75.
2. Klose T, Leidl R, Buchmann I, Brambs HJ, Reske SN. Primary staging of lymphomas: cost-effectiveness of FDG-PET versus computed tomography. Eur J Nucl Med 2000;27(10): 1457–64.
3. Schaefer NG, Hany TF, Taverna C, Seifert B, Stumpe KD, von Schulthess GK, et al. Non-Hodgkin lymphoma and Hodgkin disease: coregistered FDG PET and CT at staging and restaging: do we need contrast-enhanced CT? Radiology 2004;232(3):823–9.
4. Kostakoglu L, Goldsmith SJ. Fluorine-18 fluorodeoxyglucose positron emission tomography in the staging and follow-up of lymphoma: is it time to shift gears? Eur J Nucl Med 2000;27(10): 1564–78.
5. Hany TF, Steinert HC, Goerres GW, Buck A, von Schulthess GK. PET diagnostic accuracy: improvement with in-line PET-CT system: initial results. Radiology 2002;225(2):575–81.
6. Schiepers C, Filmont JE, Czernin J. PET for staging of Hodgkin's disease and non-Hodgkin's lymphoma. Eur J Nucl Med Mol Imaging 2003;30:Suppl 1:S82–8.
7. Stumpe KD, Urbinelli M, Steinert HC, Glanzmann C, Buck A, von Schulthess GK. Whole-body positron emission tomography using fluorodeoxyglucose for staging of lymphoma: effectiveness and comparison with computed tomography. Eur J Nucl Med 1998;25(7):721–8.
8. Hoskin PJ. FDG PET in the management of lymphoma: a clinical perspective. Eur J Nucl Med Mol Imaging 2002; 29(4):449–51.
9. Spaepen K, Stroobants S, Verhoef G, Mortelmans L. Positron emission tomography with [(18)F]FDG for therapy response monitoring in lymphoma patients. Eur J Nucl Med Mol Imaging 2003;30:Suppl 1:S97–105.
10. Segall GM. FDG PET imaging in patients with lymphoma: a clinical perspective. J Nucl Med 2001;42(4):609–10.
11. Schoder H, Meta J, Yap C, Ariannejad M, Rao J, Phelps ME, et al. Effect of whole-body (18)F-FDG PET imaging on clinical staging and management of patients with malignant lymphoma. J Nucl Med 2001;42(8):1139–43.
12. Jerusalem G, Beguin Y, Fassotte MF, et al. Whole-body positron emission tomography using 18F-fluorodeoxyglucose for posttreatment evaluation in Hodgkin's disease and non-Hodgkin's lymphoma has higher diagnostic and prognostic value than classical computed tomography scan imaging. Blood 1999;94(2):429–33.
13. Spaepen K, Stroobants S, Dupont P, Vandenberghe P, Maertens J, Bormans G, et al. Prognostic value of pretransplantation positron emission tomography using fluorine 18-fluorodeoxyglucose in patients with aggressive lymphoma treated with high-dose chemotherapy and stem cell transplantation. Blood 2003;102(1):53–9.
14. Beyer T, Townsend DW, Brun T, Kinahan PE, Charron M, Roddy R, et al. A combined PET/CT scanner for clinical oncology. J Nucl Med 2000;41(8):1369–79.
15. Reinartz P, Wieres FJ, Schneider W, Schur A, Buell U. Side-by-side reading of PET and CT scans in oncology: which patients might profit from integrated PET/CT? Eur J Nucl Med Mol Imaging 2004;31(11):1456–61.
16. Freudenberg LS, Antoch G, Schutt P, et al. FDG-PET/CT in re-staging of patients with lymphoma. Eur J Nucl Med Mol Imaging 2004;31(3):325–9.
17. Schoder H, Larson SM, Yeung HW. PET/CT in oncology: integration into clinical management of lymphoma, melanoma, and gastrointestinal malignancies. J Nucl Med 2004;45: Suppl 1:72S–81S.
18. von Schulthess GK, Steinert HC, Hany TF. Integrated PET/CT: Current applications and future directions. Radiology 2006;238(2):405–22.
19. Nakamoto Y, Sakamoto S, Okada T, et al. Accuracy of image fusion using a fixation device for whole-body cancer imaging. AJR Am J Roentgenol 2005;184(6):1960–6.
20. Diederichs CG, Staib L, Glatting G, Beger HG, Reske SN. FDG PET: elevated plasma glucose reduces both uptake and detection rate of pancreatic malignancies. J Nucl Med 1998; 39(6):1030–3.
21. Tatsumi M, Kitayama H, Sugahara H, Tokita N, Nakamura H, Kanakura Y, et al. Whole-body hybrid PET with 18F-FDG in the staging of non-Hodgkin's lymphoma. J Nucl Med 2001;42(4):601–8.
22. Tatsumi M, Cohade C, Nakamoto Y, Fishman EK, Wahl RL. Direct comparison of FDG PET and CT findings in patients with lymphoma: initial experience. Radiology 2005;237(3): 1038–45.
23. Carbone PP, Kaplan HS, Musshoff K, Smithers DW, Tubiana M. Report of the committee on Hodgkin's disease staging classification. Cancer Res 1971;31(11):1860–1.
24. Delbeke D. Oncological applications of FDG PET imaging: brain tumors, colorectal cancer, lymphoma and melanoma. J Nucl Med 1999;40(4):591–603.
25. Hoffmann M, Kletter K, Diemling M, Becherer A, Pfeffel F, Petkov V, et al. Positron emission tomography with fluorine-18-2-fluoro-2-deoxy-D-glucose (F18-FDG) does not visualize extranodal B-cell lymphoma of the mucosa-associated lymphoid tissue (MALT)-type. Ann Oncol 1999;10(10):1185–9.
26. Karam M, Novak L, Cyriac J, Ali A, Nazeer T, Nugent F. Role of fluorine-18 fluoro-deoxyglucose positron emission tomography scan in the evaluation and follow-up of patients with low-grade lymphomas. Cancer 2006;175:183.